Invited Review

Applications of Free-Electron Lasers in the Biological and Material Sciences[¶]

G. S. Edwards*[1], S. J. Allen[2], R. F. Haglund[3], R. J. Nemanich[4], B. Redlich[5], J. D. Simon[6] and W.-C. Yang[4]

[1]Physics Department, Duke University, Durham, NC
[2]Physics Department, University of California, Santa Barbara, CA
[3]Department of Physics and Astronomy, Vanderbilt University, Nashville, TN
[4]Department of Physics and Department of Materials Science and Engineering,
 North Carolina State University, Raleigh, NC
[5]FELIX, FOM Institute for Plasma Physics, Nieuwegein, The Netherlands
[6]Departments of Chemistry, Biochemistry, and Ophthalmology, Duke University, Durham, NC

ABSTRACT

Free-Electron Lasers (FELs) collectively operate from the terahertz through the ultraviolet range and via intracavity Compton backscattering into the X-ray and gamma-ray regimes. FELs are continuously tunable and can provide optical powers, pulse structures and polarizations that are not matched by conventional lasers. Representative research in the biological and biomedical sciences and condensed matter and material research are described to illustrate the breadth and impact of FEL applications. These include terahertz dynamics in materials far from equilibrium, infrared non-linear vibrational spectroscopy to investigate dynamical processes in condensed-phase systems, infrared resonant-enhanced multiphoton ionization for gas-phase spectroscopy and spectrometry, infrared matrix-assisted laser-desorption–ionization and infrared matrix-assisted pulsed laser evaporation for analysis and processing of organic materials, human neurosurgery and ophthalmic surgery using a medical infrared FEL and ultraviolet photoemission electron microscopy for nanoscale characterization of materials and nanoscale phenomena. The ongoing development of ultraviolet and X-ray FELs are discussed in terms of future opportunities for applications research.

Abbreviations: 2-MP, 2-methylpentane; BSA, bovine serum albumin; CH_2Cl_2, dichloromethane; CO, carbon monoxide; CO_2, carbon dioxide; CPGE, circular photogalvanic effect; CVD, chemical vapor deposition; CW, continuous wave; DBP, dibutyl pthalate; DC, direct current; DESY, Deutsches Elektronen-Sychrotron; DFT, density-functional theory; EDTA, ethylenediaminetetraacetic acid; Er:YAG, erbium yttrium-aluminum-garnet; Fe, iron; FEL, free-electron laser; FELICE, free-electron laser for intracavity experiments; FELIX, free-electron laser for infrared experiments; FTICR-MS, Fourier-transform ion-cyclotron mass spectrometer; FTIR, Fourier-transform infrared; GaN, gallium nitride; HEDTA, hydroxyethyl ethylenediamine triacetic acid; H–Si, hydrogen–silicon; IgG, immunoglobulin G; InGaAs, indium gallium arsenide; IR-IDS, infrared ion-dip spectroscopy; IR-MAPLE, infrared matrix-assisted pulsed-laser evaporation; IR-MPD, infrared multiphoton dissociation; IR-REMPI, infrared resonance-enhanced multiphoton ionization; ISO, Infrared Space Observatory; LCLS, linac coherent light source; MALDI-MS, matrix-assisted laser desorption–ionization mass spectrometry; MBE, molecular beam epitaxy; Met-Car, metallo-carbohedrenes; MOS, metal-oxide-semiconductor; 2-MTHF, 2-methyltetrahydrofuran; N, nitrogen; NH_2, amino group; NHE, normal hydrogen electrode; OK, optical klystron; OR, Ostwald ripening; Os, osmium; PEEM, photoemission electron microscopy; PIMBE, plasma-induced molecular beam epitaxy; PLD, pulsed-laser deposition; post-AGB, postasymptotic giant branch; PVG, physical vapor deposition; Rh, rhodium; RPE, retinal pigment epithelium; Ru, ruthenium; SASE, self-amplified spontaneous emission; SCA, superconducting linear accelerator; SGE, spin-galvanic effect; Si, silicon; SIO_2, silica; SiO_x, silicon oxide; SS, surface states; TESLA, TeV-energy superconducting linear accelerator; Ti, titanium; $TiSi_s$, titanium silicide; UCSB, University of California, Santa Barbara; UHV, ultrahigh vacuum; vis, visible; $W(CO)_6$, tungsten hexacarbonyl.

INTRODUCTION

Free-electron lasers (FELs) convert the kinetic energy of electrons into light (1,2). A schematic diagram is shown in Fig. 1. An accelerator produces ''free'' electrons at relativistic speeds in a vacuum. These electrons pass through a ''wiggler'' field, a periodic magnetostatic field, in an optical cavity. The essential feature of FELs is that the light propagating along the axis is amplified and the kinetic energy of the electrons is decremented when the wiggler deflects the electrons into a serpentine path. Experimental realizations of FELs are based on a series of accelerator technologies, operating with electron energies from as low as keV and up to GeV. Collectively FELs operate from the microwave through the X-ray wavelengths; however, each accelerator technology corresponds to a restricted wavelength range of operation. Shorter wavelengths are achievable by harmonic generation and X-rays and gamma rays have been produced by intracavity Compton backscattering. Numerous
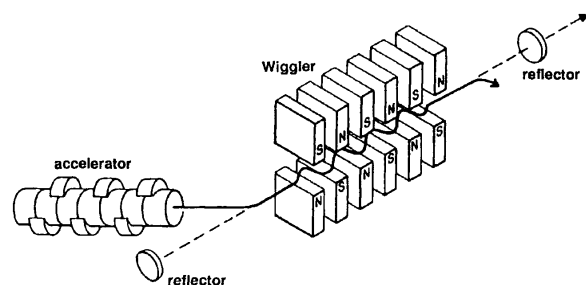
Figure 1. The basic scheme for an FEL. An accelerator produces an electron beam that is steered through a wiggler under vacuum. Two reflectors, external to the wiggler, define an optical cavity. In this example, there is one total reflector and one partial reflector.

reviews of FEL physics are available (3–8). FELs have been commissioned in many countries at universities, national laboratories and in the private sector. FEL technology continues to be developed at both ends of the spectrum, toward shorter femtosecond pulse durations and with selectively variable polarization. Many FELs have become quite reliable during the past 2 decades, typically producing several thousands of hours per year of user time.

FELs are versatile and in some cases unique light sources that support applications research by a broad user community. Because the wavelength of the emitted light depends on the energy of the electrons and the properties of the magnetic field, an FEL can be tuned within its wavelength range of operation with relative ease. Whereas the lasing medium for FELs is the free beam of electrons, the lasing medium for conventional lasers is bound electrons and the accompanying atomic nuclei, which restricts laser performance. For FELs, waste heat is carried away as the electrons pass out of the wiggler. Consequently, FELs can operate in wavelength ranges in which conventional lasers cannot operate and can have optical power, pulse and polarization characteristics that conventional lasers have not achieved. The FEL optical pulse structure correlates with the bunching of the electron beam whereas the polarization is determined by the magnetic field. Some FELs continuously produce optical pulses at a set repetition rate. Other FELs have a complex optical pulse structure with a burst (macropulse) of micropulses. The micropulse lifetime can be picoseconds or shorter and the micropulse repetition rate within a macropulse can be as high as gigahertz. The repetition rate of the macropulse can be as high as many tens of Hertz.

We review FEL applications research in the biological and material sciences. We emphasize applications that uniquely take advantage of FELs and also have had a scientific or technological impact independent of FEL physics. This user community currently includes physical scientists working on physical research problems as well as multidisciplinary teams investigating interdisciplinary research. Additional areas of FEL applications research have been reviewed elsewhere (9–14); taken together one gets a better appreciation of the overall FEL research enterprise and its potential.

The following sections present representative examples that illustrate the breadth of FEL applications research in the biological and material sciences. The presentation is organized according to wavelength of operation, including the terahertz FELs at the University of California, Santa Barbara (UCSB); the infrared FELs in The Netherlands and at Duke, Stanford and Vanderbilt

Universities; and the ultraviolet FEL at Duke University. We conclude with a consideration of emerging applications based on FEL light source development. We will not delve into FEL technology, instead emphasizing applications research and those operating characteristics of various FELs that have enabled scientific advancements in material and condensed matter research and the biological and biomedical sciences.

An aim of this review is to introduce photochemists and photobiologists to the research opportunities of current and future FELs. Typically past FEL applications research has been initiated with a narrowly defined project; however, once successfully pioneered, the technique and supportive infrastructure have become tools for a broader range of interdisciplinary research. FEL research tends to be multidisciplinary, including accelerator physicists developing the light source collaborating with physical, biological and biomedical scientists pursuing applications research. Hopefully this review will encourage additional photochemists and photobiologists to consider and pursue FEL applications research. With this in mind, in the following we review FEL applications research in the biological and material sciences. Several themes will be apparent: the competition between dynamical processes and the influence FELs can have on the outcome, the light source frontiers accessed by FELs and how they enable novel spectroscopic and imaging techniques as well as processing of (bio)materials and spin-off technology due to FEL-based research.

MATERIAL SCIENCE WITH TERAHERTZ FELS

The terahertz region of the electromagnetic spectrum is a rich arena for research in physics, chemistry, biology, material science and medicine. Historically, exploring science in the terahertz region of the spectrum has proved challenging because of the lack of commercial light source technology. Commercial electronic sources have only advanced to hundreds of gigahertz whereas commercial solid-state photonic sources have only extended wavelengths to $\sim$30 μm (10 THz). The challenge has been met with a variety of laboratory sources ranging from short-pulse terahertz beams to molecular gas lasers to backward wave oscillators to Fourier-transform infrared spectroscopy (FTIR) to FELs. Each brings characteristic strengths and limitations. The ''unfair advantage'' of terahertz FELs lies in their high power and tunability. The FELs at UCSB operate from 0.14 to 4.8 THz ($\sim$4.6–160 cm^{-1} or a wavelength of 2 mm to 60 μm). These light sources are quasicontinuous wave (quasi-CW), with pulse durations of 2–20 μs; have high peak power, ranging from 500 W to 10 kW; and produce modest average powers of tens of milliwatts. The average fractional linewidth is approximately 5×10^{-4}, determined by stochastic start-up on each pulse. Single-pulse fractional linewidth can be as narrow as 5×10^{-7} depending on mode structure. Pulse repetition rate can be as high as 7.5 Hz.

During the past decade, FELs have been vital to the successful exploration of terahertz dynamics in materials, especially dynamics driven far from equilibrium by strong terahertz fields. Advances have been made in electro-optics, coherent quantum control, photon-assisted transport, material physics, device physics and nonequilibrium dynamics (15). We highlight a few examples of advances in terahertz electro-optics, coherent quantum control and material physics. In each case, we outline those features of terahertz FELs that open new research vistas, primarily frequency, tunability and power.
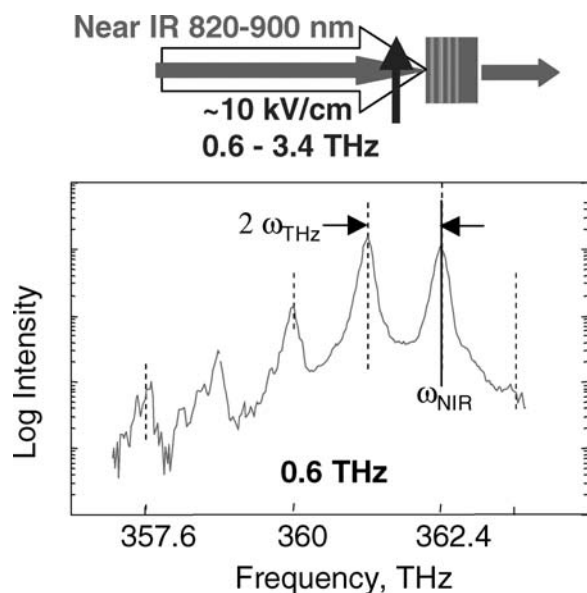
Figure 2. Collinear near-IR and terahertz radiation exit the InGaAs quantum well semiconductor with sidebands separated by twice the terahertz frequency.

Figure 3. Fifty asymmetric coupled quantum wells break the symmetry and allow sidebands separated by an odd multiple of the terahertz modulation at 1.5 THz. Sideband generation is enhanced as the near-IR and terahertz radiation resonate interband and intersubband transitions. Reprinted with permission from reference 19.

Terahertz electro-optics

Control of light propagation in materials and material structures by applied electric fields is a powerful probe of the properties of materials in addition to being a fundamental building block of modern communication and information processing. The term ''electro-optics'' usually describes the modification of the optical properties by direct current (DC) or slowly varying fields. However, at terahertz frequencies the applied electric field—the controlling electric field—is not ''slowly varying.'' The dynamics of the material system become important; terahertz frequencies exceed the relaxation rates of most interesting material systems, and material resonances alter the electro-optics in fundamental ways.

Dynamical Franz-Keldysh effect. The Franz-Keldysh effect (16,17) describes the result of a DC electric field on the absorption of light in a semiconductor at the ''band edge'' at frequencies that excite an electron from the filled valence band to the empty conduction band. At terahertz frequencies and large terahertz electric fields, the interaction is called the ''dynamical Franz-Keldysh effect.'' This regime is defined by

$$e\left(\frac{eE_{THz}}{m^*\omega_{THz}^2}\right)E_{THz} > \hbar\omega_{THz} \tag{1}$$

where e is the electron charge; m^* is the effective mass; ω_{THz} is the terahertz frequency; E_{THz} is the terahertz field strength; and $\hbar$ is Planck's constant.

The quantity $(eE_{THz}/m^*\omega_{THz}^2)$ describes the free motion of an electron in the terahertz field and is only relevant if $\omega_{THz}\tau > 1$. The damping of the electron motion is small and ignored to first order. In the limit of small or negligible damping, the electron's motion is said to be dynamic; if the frequency is low and/or the damping rate $1/\tau$ is fast, the electron motion is diffusive. In most semiconductor systems, electron motion becomes dynamic at terahertz frequencies. But arbitrarily high frequencies require, by inspection of (Eq. 1), arbitrarily high electric fields and power. The terahertz regime is the lowest frequency regime in which this phenomenon emerges.
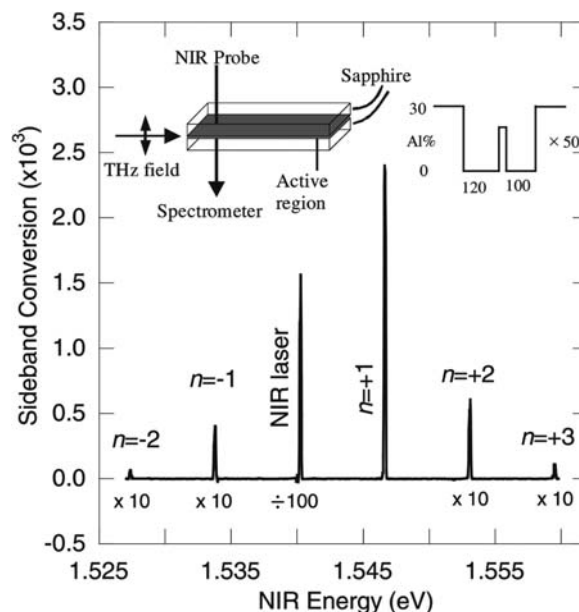
The modulation of the "band edge" absorption by the intense terahertz electric fields results in new optical beams at frequencies separated from the incident laser beam by multiples of the terahertz frequency. Figure 2 shows the spectrum of near-IR radiation that exits an indium gallium arsenide (InGaAs) semiconductor, pseudomorphically grown on GaAs as multiquantum wells. Symmetry rigorously enforces ''even'' sidebands. Sidebands are separated from the near-IR frequency by even multiples of the terahertz frequency up to $8 \times \omega_{THz}$.

Resonant terahertz sideband generation. These effects are dramatically enhanced if the terahertz radiation resonates with internal quantum mechanical transitions. Excitonic features dominate the absorption of light at the band edge. An exciton describes a photoexcited electron that continues to be bound to the positively charged ''hole'' that it vacated. The terahertz radiation shifts the frequency of the exciton absorption line up and down as the terahertz radiation is brought into resonance with the internal transitions of the excitons (18).

By engineering material structures, for example, by introducing multiquantum well superlattices, the modulation of the optical light by terahertz radiation can be enhanced many orders of magnitude (19). Terahertz radiation that resonates with internal transitions in the quantum wells produces enhanced modulation of the incident light. Sideband generation is resonantly enhanced as the terahertz radiation resonates with quantum transitions in the exquisitely crafted semiconductor nanostructures, as shown in Fig. 3. More important, the symmetry can be broken in a controlled fashion and sidebands can be generated that are separated from the near-IR frequency by an odd multiple of the terahertz frequency.

Coherent quantum control

As noted above, the electron motion at terahertz frequencies in semiconductor quantum structures is dynamic, that is it follows the oscillations of the terahertz fields for many cycles before it relaxes
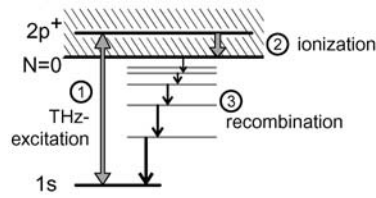
Figure 4. Left: Energy levels of a donor in a magnetic field. Electrons are excited coherently by terahertz radiation and undergo Rabi oscillations between the excited state and ground state. Excited population is sensed by measuring the current caused by ionization, process 2 in the figure from the excited state. Right: The excited state population as monitored by the induced current undergoes Rabi oscillations as a function of terahertz pulse duration and parameterized by resonance detuning. Reprinted with permission from reference 20.
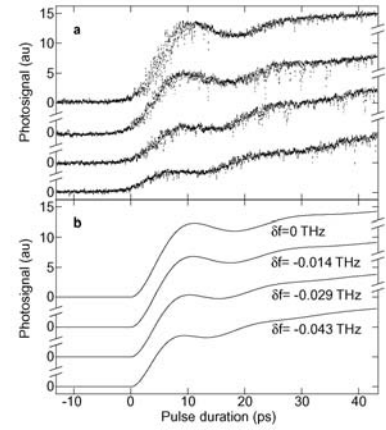
or is scattered; quantum mechanically speaking, intense terahertz fields can control the quantum state of the electron. The projected future of "quantum computing" relies on the control of quantum mechanical states before they relax or lose their phase coherence. In the anticipated "quantum computer," information is stored as "qubits." Despite the fast dephasing and relaxation times characteristic of electron states in condensed matter, the ultimate utility of quantum computing and information processing will hinge on coherent quantum control in solids.

Terahertz Rabi oscillations in isolated donors. The phrase "Rabi oscillation" describes the cycling of the quantum system between ground and excited states by an external high-frequency field. A two-level system undergoes Rabi oscillations when a high-frequency field is sufficiently intense that it drives the system from the ground state to the excited state and back down again before it loses quantum mechanical phase memory. Using intense terahertz radiation from the FELs and a picosecond pulse slicer, Rabi oscillations were observed between electron states in isolated donor impurities as summarized in Fig. 4. These experiments showed that hydrogen atom–like motional states of electrons bound to donor impurities can serve as model qubits (20). To make these observations, the DC photocurrent produced by terahertz excitation of the donor-bound electron was measured as a function

of the terahertz pulse duration. Rapid dephasing required controlling the pulse duration at the picosecond timescale. This is accomplished with a variable picosecond pulse slicer, engineered with solid-state plasma switches driven by a femtosecond laser system (21).

Absolute negative conductance and dynamic localization. The measurement of absolute negative conductance in terahertz-driven semiconductor superlattices is one of the most striking observations made with terahertz FELs (22,23). Much like microwaves control the tunnel current between two superconductors, radiation can control the quantum tunneling between two quantum wells in a semiconductor nanostructure. At predicted values of the frequency and field strength,

$$\frac{eaE_{\mathrm{THz}}}{\hbar\omega_{\mathrm{THz}}} = \zeta \qquad (2)$$

where a is the quantum well spacing and ζ is the zero of the 0th-order Bessel function, electrons can only quantum tunnel by absorbing or emitting a photon. They are said to be dynamically localized (24). However, when they are stimulated to absorb or emit a photon they move from one quantum well to the next or up and down the Stark ladder as the Stark ladder splitting is less or greater than the photon energy. For small voltages or fields, electrons move up the ladder and exhibit absolute negative conductance, as shown in Fig. 5.

The terahertz regime is uniquely suited to explore these phenomena. The electron motion must be dynamic, $\omega_{\mathrm{THz}}\tau > 1$. Although this condition is satisfied for much higher frequencies, Equation 2 indicates that the required power scales like the frequency and catastrophic heating by radiation is harder to avoid. The nonequilibrium dynamics described here appear without severe material heating only at terahertz frequencies.

Material physics

The high power of the FEL is not particularly useful for linear spectroscopy unless the throughput is particularly low. In contrast, when the throughput is high, linear terahertz spectroscopy is better accomplished with more conventional sources such as Fourier-transform spectroscopy, time-domain spectroscopy or molecular gas lasers.

Stark-ladder spectroscopy. A multiquantum well superlattice in a DC electric field is described as a Stark ladder. The energies of the quantum states are separated by eaE_{DC}, the voltage drop
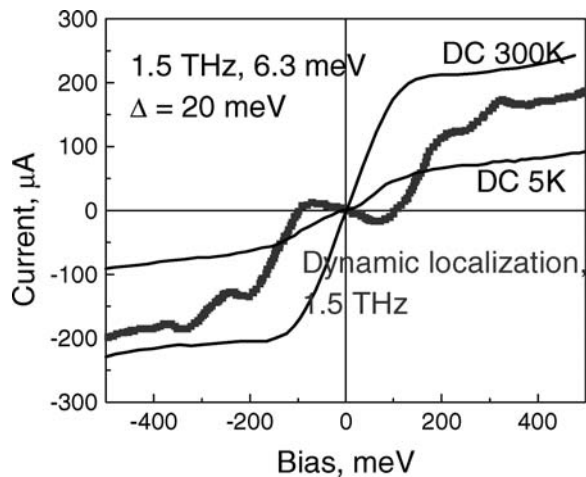

Figure 5. Electron transport through a semiconductor superlattice exhibits absolute negative conductance when dynamically localized by an intense terahertz electric field of given strength (Eq. 2).
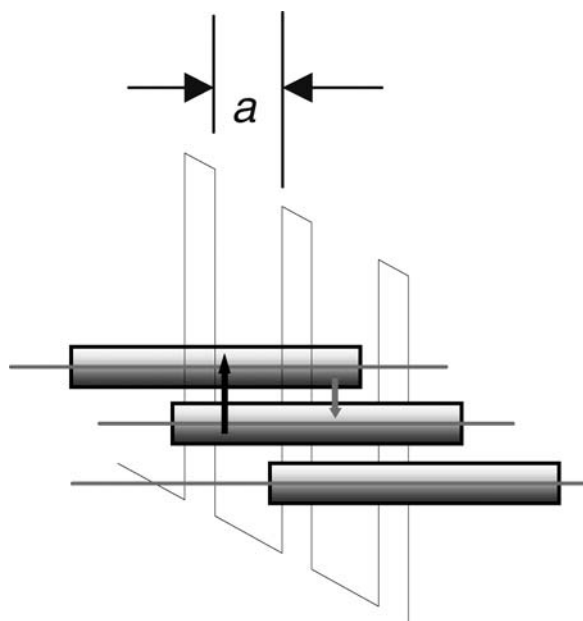
Figure 6. A semiconductor superlattice in an electric field produces a Stark ladder. Terahertz radiation drives electrons up or down the ladder as the photon energy is greater than or less than the Stark splitting.

Figure 7. a: A superlattice mesa. b: Radiation from the UCSB free-electron lasers is focused onto the 10-μm high opening of the terahertz waveguide and guided to the entrance aperture of the detector. c: Waveguide with top metal/contact removed exposing sidewall confinement by photonic band gap structure and an array of superlattice posts. Reprinted with permission from reference 25.

between neighboring wells, and form the ''rungs'' of the ladder. The linear dynamical response of the Stark ladder in an electrically biased superlattice is intimately related to the dynamic localization described above (25). Dynamic localization manifests itself as a dramatic change in DC conductance when the superlattice is irradiated with terahertz radiation. The linear dynamical conductivity $\sigma(\omega_{THz})$ is more difficult to measure but critically important for the use of electrically biased superlattices in future terahertz electronics.

A weak terahertz field can be amplified if the frequency is less than the Stark ladder splitting, as summarized in Fig. 6. This gain may be potentially important for making a tunable terahertz oscillator. To measure the dynamical conductance of subwavelength mesas, an array of superlattice posts was inserted in a terahertz waveguide only 10-μm high (Fig. 7). The top and bottom of the waveguide allowed electrical bias of the array while radiation from the UCSB FELs was guided to a sensitive detector. The high terahertz power of the FELs overcomes the very small throughput caused by the narrow entrance aperture of the waveguide.

Figure 8 shows the crossover from loss to gain at 1.98 THz in the superlattice material as the electrical bias causes the Stark ladder splitting to exceed the photon energy. Although this is a measurement of the linear terahertz response, the small throughput makes this experiment impossible without the relatively high power from the FEL. These experiments open the possibility of solid-state terahertz oscillators based on electrically biased superlattices in terahertz cavities.

Terahertz circular dichroism in biopolymers. Circular dichroism describes the difference in absorption or propagation of right- and left-handed radiation in material. It is a signature of chirality and has been well-characterized and used in the visible, UV and near-IR frequencies in various biopolymer materials. Circular dichroism has not been explored or exploited at terahertz frequencies. Biopolymer excitations at terahertz frequencies are particularly
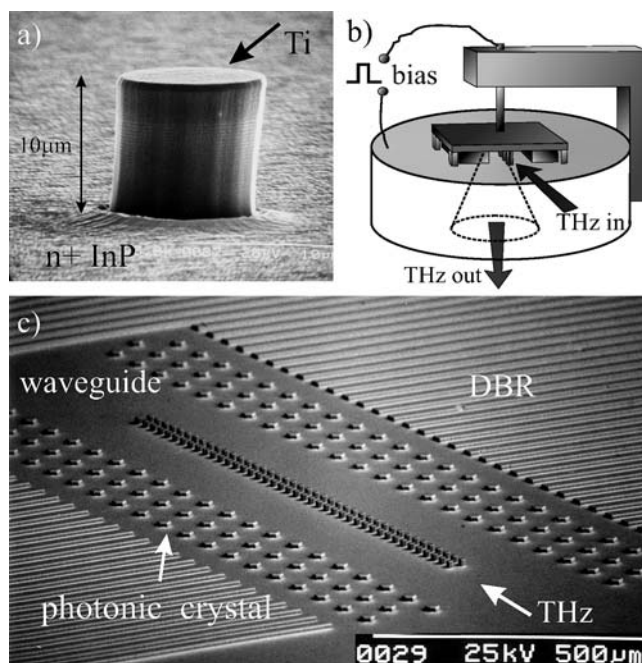
important because they describe small-amplitude macromolecular motions that are the precursors of functionally relevant, large-amplitude conformational changes. In principle, terahertz circular dichroism can sense the biopolymer motions free of the background absorption from nonbiological material.

Terahertz circular dichroism in aqueous biopolymers requires tunable, high-power sources to measure what is essentially the linear response of this material but in the presence of very strong background absorption. Toward this end, a polarization articulated interferometer has been developed (Fig. 9). When driven by the coherent, high-power radiation of the FEL, terahertz circular
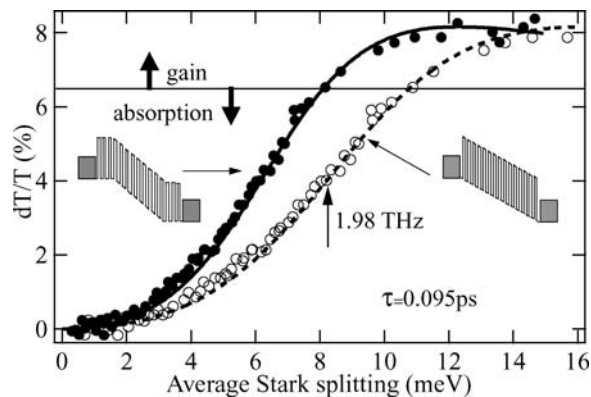

Figure 8. Change in transmission through the waveguide at 1.98 THz as function of electrical bias indicates a crossover from loss to gain as the Stark ladder splitting exceeds the terahertz photon energy. Reprinted with permission from reference 25.
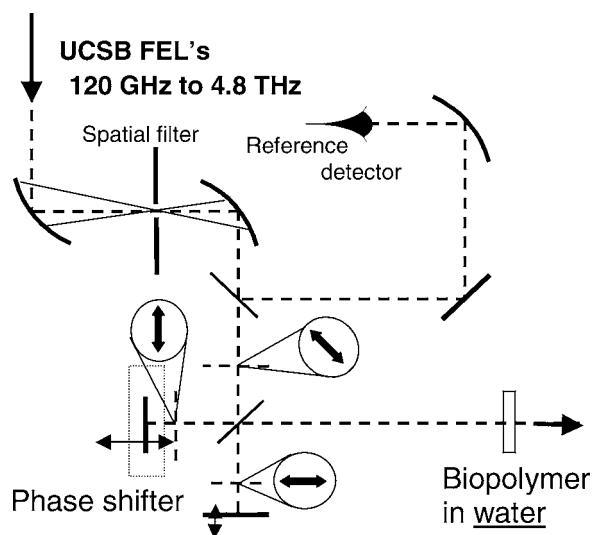
Figure 9. A polarization articulated interferometer modulates the terahertz radiation between right and left handed circular polarization.

dichroism has been detected in concentrated solutions of lysozyme. A work in progress, this capability depends on the spectral coherence and high power of terahertz FEL (26,27).

Current and future enhancements of the UCSB terahertz FEL

The application of injection locking to narrow the average linewidth is under study and will be attempted as technology permits. In addition, although the terahertz FELs operate at any frequency within their range, the ease of continuous tunability is limited to several percent by the need to resteer the electron beam. A new control system is under development based on an expert system and concepts of artificial intelligence to automate operator functions.

Summary of terahertz FEL applications

The high power and tunability of terahertz FELs has enabled the exploration of terahertz dynamics in systems driven far from equilibrium. It would be virtually impossible to have carried out these experiments with other terahertz-source technology. In addition, there are circumstances in which the high power makes possible experiments in the linear regime, *i.e.* experiments in which the throughput is very small and the high power substantially improves the signal-to-noise ratio.

Terahertz FELs have enabled advances in electro-optics, coherent quantum control, photon-assisted transport, material physics, device physics and nonequilibrium dynamics. There is a repeating theme in the wide variety of terahertz phenomena in semiconductor structures—at terahertz frequencies classical or quantum dynamics rather than relaxation, drift and diffusion dominate the material and device physics. Combined with high-terahertz power a totally new regime of dynamic nonequilibrium in semiconductor quantum structures is revealed.

NONLINEAR VIBRATIONAL SPECTROSCOPY IN THE CONDENSED PHASE WITH THE INFRARED SCA FEL

The superconducting linear accelerator (SCA) FEL at Stanford is an enabling source for nonlinear vibrational spectroscopy. The

SCA FEL is broadly tunable in the mid-IR frequencies (3–15 μm), producing micropulses with a duration of 0.7–3 ps at a repetition rate of 11.8 MHz and a micropulse energy of microjoules. The effective experimental micropulse repetition rate can be reduced to kilohertz by an acousto-optic modulator system. The macropulse duration is 2 ms and the macropulse repetition rate can be as high as 20 Hz. The spectral bandwidth is transform-limited with a stability of 0.01% rms. The amplitude stability is less than 2% rms. Vibrational photon-echo techniques have been developed with use of the SCA FEL (28). Together with pump-probe and transient-grating measurements, these techniques have been used to advance the understanding of vibrational dynamics in liquids and glasses where the homogeneous vibrational line shape is extracted from an otherwise inhomogeneously broadened mid-IR spectral feature. In particular, these techniques have been used to investigate intermolecular and intramolecular dynamics that give rise to homogeneous linewidths and pure dephasing of the asymmetric carbon monoxide (CO) stretching modes of metal carbonyl solutes in several glassy and liquid solvents (29,30) as well as the CO ligand in native and mutant myoglobins (31). For this and other studies of dynamical processes in condensed-phase systems, the American Physical Society awarded Michael Fayer the Earl K. Plyler Prize for Molecular Spectroscopy in March 2000.

The vibrational homogeneous linewidth is an experimental observable of the vibrational photon-echo measurement. The scientific foundation of the echo technique lies in the spin echo of magnetic resonance (32), first described by Hahn in 1950 (33). The optical photon echo was demonstrated in 1964 (34,35) and has been used since then to investigate electronic excited-state dynamics. The echo is a consequence of two pulses separated in time, and in the case of vibrational photon echoes, the first IR pulse excites an ensemble of solute molecules into a superposition state of vibrational levels. The microscopic dipoles are in phase immediately after the first pulse. Because there is a distribution of vibrational frequencies, the phase coherence rapidly decays. The second IR pulse arrives at an angle θ with respect to the trajectory of the first pulse, with a delay τ, and initiates a rephasing process reminiscent of time reversal. At a time τ after the second pulse, a coherent pulse is emitted, *i.e.* an IR or vibrational photon echo. The echo is emitted at an angle 2θ with respect to the first pulse because of matching wave vectors. Although the rephasing process overcomes inhomogeneous broadening, fluctuations compromise the rephasing process and with increasing τ the intensity of the echo decreases. A decay of the echo intensity as a function of τ in effect measures the fluctuations in the vibrational frequencies. Consequently, the Fourier transform of the echo decay curve is the homogeneous line shape.

In the pump-probe experiments, ~90% of the IR pulse serves as a pump and ~10% as a probe, where the probe pulse is delayed by τ. The pump pulse bleaches the sample, and the probe pulse measures the recovery as a function of τ. In the transient-grating experiment, the IR pulse is divided into three pulses, one of which is delayed by τ. The two coincident pulses are crossed in the sample to produce an interference pattern, which leads to a diffraction grating in the population of excited vibrational modes. Because the delayed pulse will diffract from the population diffraction grating at the Bragg angle, measurements as a function of τ will determine the lifetime of the excited vibrational modes. In both experiments, polarized pulses can be used to distinguish orientational relaxation from lifetime relaxation.
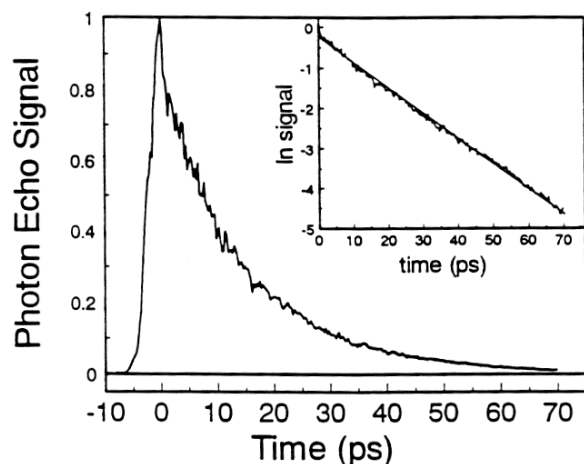
Figure 10. Vibrational photon echo decay data taken of W(CO)$_6$ in 2-MTHF at 16 K. The inset is a semilogarithmic plot showing the data decay exponentially. Reprinted with permission from reference 28.

Metal carbonyl solutes in glassy and liquid solvents

Vibrational photon echo, pump-probe and transient-grating experiments of the asymmetric CO-stretch mode of tungsten hexacarbonyl (W[CO]$_6$) in various solvents have provided a foundation for understanding the dynamics of molecular vibrations in condensed-matter systems. The seminal experiment investigated the asymmetric CO-stretch mode of W(CO)$_6$ in 2-methyltetrahydrofuran (2-MTHF) (28). The FEL was tuned to 5.10 μm and the micropulse duration was 2.7 ps at a repetition rate of 1 kHz. Because the coupling of vibrations to the heat bath, *i.e.* mechanical degrees of freedom external to the molecule, is substantially weaker than that of electronic states, the dephasing times are relatively long for the vibrational photon echo, and there are little or no solvation dynamics. Consequently, picosecond pulses are appropriate for this investigation. The temperature was varied from 300 to 16 K, taking the sample from a liquid to a supercooled liquid and then to a glass. Photon echoes were observed from 16 to 140 K, where T$_g$ is 90 K, and the photon-echo decay curve at 16 K is shown in Fig. 10. The time constant for the decay is 15 ps, the homogeneous dephasing time is 60 ps and the homogeneous linewidth is 5.2 GHz, which should be compared with the inhomogeneous linewidth of 540 GHz. The pure dephasing time contribution to the homogeneous linewidth, a measure of the influence of conformational fluctuations on the vibrational energy level spacing, is 1.6 GHz.

Subsequent measurements investigated W(CO)$_6$ in 2-methylpentane (2-MP) from room temperature to 10 K (36). The FEL was tuned to 5.04 μm, and the pulse duration was ∼1.5 ps. These results suggest that the asymmetric CO-stretch mode can be inhomogeneously broadened in liquid solutions and that inhomogeneous broadening occurs at room temperature. The apparent decay time was 1.6 ps, the homogeneous linewidth was 49 GHz and the inhomogeneous linewidth was ∼300 GHz. The room temperature observation of the photon echo is attributable to the relatively sharp homogeneous linewidth of asymmetric CO-stretch mode for W(CO)$_6$ in 2-MP.

Infrared photon-echo beats have been observed with ∼700 fs FEL micropulses to investigate the asymmetric CO-stretching mode of W(CO)$_6$ in dibutyl pthalate (DBP) (37). The FEL can populate higher vibrational levels when the bandwidth or Rabi frequency of the micropulse exceeds the vibrational anharmonicity.
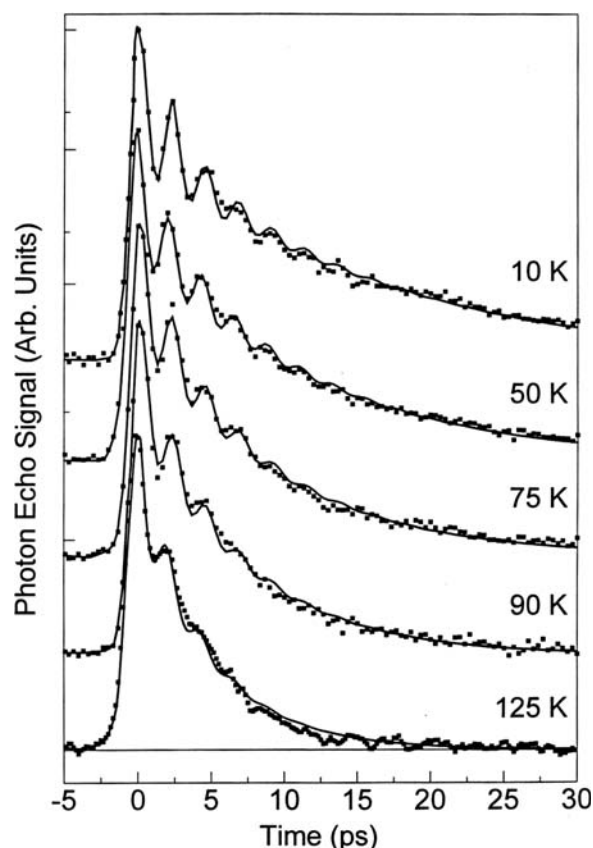

Figure 11. Beating evident in photon echo decays and fits for the asymmetric CO-stretching mode for W(CO)$_6$ in DBP as a function of temperature. Reprinted with permission from reference 37.

The beats are interpreted as multilevel coherence of the anharmonic oscillator. Figure 11 exhibits beats in the photon-echo decay curve, which are accounted for by a three-level model with a modulation frequency of 2.3 ps and a vibrational anharmonic splitting of 14.7 ± 0.3 cm^{-1}.

Vibrational spectral diffusion has been investigated with pump-probe and transient-grating techniques using 1.3 ps pulses from the FEL and 10 ps pulses from an optical parametric amplifier (38). An ensemble of solute molecules will sample all possible solvent environments and thus a distribution of transition energies on some timescale. Consequently, the homogeneous line spectrally diffuses throughout the full inhomogeneous line on a timescale that is long with respect to the homogeneous dephasing time. Measurements of a transient spectral hole demonstrate spectral diffusion and orientational motion of the asymmetric CO-stretching mode for W(CO)$_6$ in 2-MP. Intriguingly, the lifetime increases with temperature.

Native and mutant myoglobins

Investigation of the dynamics of the CO-stretching mode in myoglobin has provided insight into protein dynamics (39). Myoglobin stores and transports O$_2$ in muscle tissue. CO or O$_2$ binds to the iron atom located in a symmetric protoheme, *i.e.* iron(II) protoporphyrin-IX, located in the myoglobin interior. Myoglobin has a number of conformational substates and conformational dynamics of proteins occur over a wide variety of timescales. The FEL was used for pump-probe measurements of

the vibrational lifetime of the CO-stretching mode in myoglobin and water soluble, bare Fe:porphyrin near 5.1 μm as a function of solvent and temperature (40). The lifetime was relatively insensitive to temperature over the range of 20 to 300 K, indicating that vibrations with frequencies <400 cm^{-1} are relatively unimportant for relaxation of the CO-stretching mode. The lifetimes of the CO-stretching mode did depend on substrate and solvent with values of tens of picoseconds. Vibrational relaxation was slower when CO is unhindered by the local environment and faster when CO is hindered by local interactions. Measurements of metalloporphyrins containing iron (Fe), ruthenium (Ru) or osmium (Os) demonstrate that the vibrational relaxation lifetime decreases with increased mass of the metal ion (41). This indicates that vibrational relaxation of the CO-stretch mode in metalloporphyrins is not dominated by transfer though porphyrin vibrations involving the central metal ion and may instead be through longer-range interactions with the porphyrin. Additional measurements of synthetic porphyrins with different proximal ligands (imidazoles and pyridines) in dichloromethane (CH_2Cl_2) (42) and of mutants that altered the local dielectric environment (43) were performed, providing further evidence that the predominant vibrational relaxation process is the intramolecular transfer from CO to the poryphrin/heme. The carbonyl vibrational lifetime was observed to decrease as the carbonyl vibrational frequency decreases. This leads to the conclusion that vibrational relaxation of the CO-stretch mode in myoglobin is dominated by through-π-bond anharmonic coupling between CO and poryphrin/heme.

Vibrational photon-echo measurements of the CO stretch in CO-myoglobin have been investigated with the FEL tuned to 5.14 μm over the temperature range of 60 to 300 K (44) and 11 to 300 K (45) in several solvents. The CO vibrational spectrum was shown to be inhomogeneously broadened at all temperatures. The low-temperature pure dephasing time exhibited a power law temperature dependence with a coefficient of 1.3 indicative of a glass for all solvents measured. As the temperature increased, solvent-specific effects were observed. For the solvent trehalose above 200 K the pure dephasing time is well described as an activated process with $\Delta E \approx 650$ cm^{-1}, whereas for glycerol/water above 185 K, it is $\Delta E \approx 1000$ cm^{-1}, attributable to differences in the viscosity of the solvents (46). Photon-echo measurements of a mutant myoglobin, in which the polar histidine was replaced by the nonpolar valine, narrowed the homogeneous pure dephasing line width by $\sim21\%$ relative to native myoglobin (47).

Future research

Vibrational spectroscopy is important because of its selectivity in interrogating well-defined mechanical degrees of freedom in molecules. The vibrational dynamics of $W(CO)_6$ in various solvents have been well characterized with nonlinear spectroscopic techniques developed with the SCA FEL as a tunable, picosecond light source. These nonlinear techniques are a significant extension of vibrational spectroscopy for condensed systems and are continuing to be developed using both FELs and emerging conventional IR light sources.

Biology is dominated by structural dynamics, *i.e.* by vibrational dynamics. The investigation of CO-myoglobin has interrogated the coupling of the CO-stretching mode to the porphyrin/heme and to the conformational landscape of the overall protein. The current prevailing view is conformational substates are rapidly sampled in proteins, where the faster fluctuations explore the conformational landscape and give rise to slower processes associated with biological function. Nonlinear vibrational spectroscopy is a very promising tool for investigating the complex dynamics in biology with the quantitative precision of the physical sciences.

CONDENSED MATTER RESEARCH AND GAS-PHASE SPECTROSCOPY USING IR FELS

The FEL infrared experiments (FELIX) in The Netherlands includes a far-IR FEL with a spectral range from 25 to 250 μm and a mid-IR FEL with a spectral range from 3 to 40 μm (48). Light from 3 to 5 μm is achieved by lasing on the third harmonic. The output consists of bursts (macropulses) of micropulses; the spacing between the micropulses is either 1 ns (1 GHz) or 40 ns (25 MHz). Using a transient optical switch it is possible to slice a single micropulse out of the pulse train with an efficiency of more than 50%. The optical characteristics are listed in Table 1.

FELIX supports a wide range of research including physics, chemistry, material science and biology. The experiments fall predominantly into two classes: (1) vibrational relaxation phenomena in condensed matter; and (2) spectroscopy of gas-phase species, (bio)molecules and clusters, either neutral or ionized. Applications research includes amorphous materials, spintronics, nanostructures and nanocrystals, biomolecules, fullerenes, clusters and complexes.

Vibrational relaxation phenomena in condensed matter

Amorphous materials. The relaxation of the stretch vibrations of hydrogen and deuterium in amorphous silicon is of substantial technological importance. Hydrogen is often used to bind to and thereby passivate defect states of amorphous silicon by reducing the concentration of charge-carrier trapping states and recombination centers. This reduction of the number of defect states significantly enhances the characteristics of this material, but the beneficial effect strongly reduces with time. Recently, it was found that the aging effect is much smaller when deuterium is used instead of hydrogen. Lifetime measurements predominantly use the 25 MHz or single micropulse mode of the FEL in view of the relaxation times involved, not only for the primary process but also for the temperature transient because of the thermalized energy. Dedicated beamlines at FELIX support four-wave mixing techniques such as transient bleaching, transient grating, and photon-echo measurements in the mid-IR and far-IR.

Experimental measurements of the relaxation time employing four-wave mixing techniques show that whereas the decay for deuterium is clearly single-exponential, it is not for hydrogen

Table 1. Characteristic operational parameters of FELIX

Tuning range	3–250 μm (3300–40 cm^{-1})
Rapid tuning	>1 octave in a minute
Micropulse repetition rate	1 ns, 40 ns, single micropulse
Macropulse repetition rate	<10 Hz
Micropulse energy	1–50 μJ
Micropulse power	<100 MW
Macropulse duration	4–8 μs
Bandwidth (adjustable)	0.4–6% (transform limited)
Polarization	$>99\%$
Beam quality	near-diffraction limited

(49,50). This observation can be related to the striking difference in energy decay channels for both cases: whereas the relaxation for hydrogen occurs mainly via an almost resonant energy transfer to the bending mode at the same site and is therefore a local event, the relaxation of deuterium primarily involves phonons, *i.e.* modes of the bulk. This nonlocalized energy release reduces the chance of breaking the hydrogen–silicon (H–Si) bond and is believed to be the main reason for the strongly reduced aging effects.

Nanostructures. The material properties of silicon/silica (Si/SiO$_2$) nanostructures, a promising material for future optoelectronic applications, also have been investigated (51). Because the dangling bonds are passivated and nonradiative recombination is effectively suppressed, silicon nanocrystals embedded in an SiO$_2$ matrix exhibit efficient photoluminescence due to quantum-confined exciton recombination. Suboxide-related centers, *i.e.* centers with a reduced oxygen concentration compared with SiO$_2$, are thought to play a crucial role in the optical properties in Si/SiO$_2$ nanostructures. In this context, silicon oxides (SiO$_x$) represent an interesting class of materials because they phase-separate into a mixture of Si and SiO. Measurements in α-SiO$_{0.1}$ (Fig. 12a) reveal fast dynamics with a lifetime of 2.8 ps at 10 K determined by transient-grating spectroscopy. From the temperature dependence of the decay rate shown in Fig. 12b it can be inferred that stimulated emission into two accepting modes is responsible for the observed decay.

Spintronics. Investigations of the spin of electrons and holes in solid-state systems reveal that the quantum mechanical properties of these systems exhibit a large variety of interesting physical phenomena. Now generally referred to as ''spintronics,'' recently there has been considerable interest in the spin of carriers in semiconductor heterostructures. To realize spintronic devices, a high spin polarization is required. To manipulate the spins with an electric field, a large controllable splitting of subbands in k-space has to be achieved, *i.e.* the so-called Rashba effect. The Rashba effect may be produced in semiconductor quantum wells for spins oriented in the plane of the quantum well. Under the same conditions, it has been shown that the spin polarization itself drives a current, which is unpolarized, without any bias. This is of interest because it may eventually be possible to reverse the effect and produce a spin polarization simply by driving an unpolarized current, *i.e.* without the need for ferromagnetic metals or magnetic semiconductors as the contacts. This observation that the spin polarization itself drives a current is called the spin-galvanic effect (SGE) and was previously demonstrated with optical excitation and the presence of an external magnetic field. The B-field was used to discriminate between SGE and the circularly polarized analogue of photon drag (which is essentially a manifestation of the momentum transfer of photons to charged carriers) called the circular photogalvanic effect (CPGE). The all-optical-induced SGE has been demonstrated (52), a key step toward the long-term goal of establishing the existence of the SGE in zero magnetic field with purely electric injection where CPGE will be irrelevant. The tunable high-power output in the mid-IR was required for resonant excitation, to obtain a measurable photocurrent and to discriminate between CPGE and SGE, thus avoiding the need for the magnetic field. The (001)-grown, n-type GaAs quantum well structures were illuminated by circularly polarized radiation at oblique incidence to generate a component of spin polarization in the well plane, and a current signal along the well perpendicular to the plane of incidence was measured. The results showed that a helicity-dependent photocurrent along one of the <110> axes is
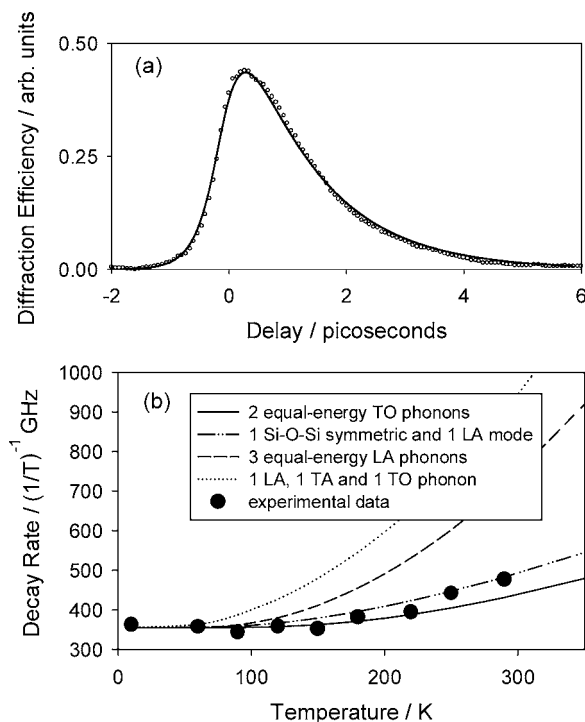

Figure 12. a: 10-K transient grating signal of α-SiO$_{0.1}$ excited via the asymmetric stretching vibration at 960 cm^{-1}. b: Temperature-dependent population decay and fits of the temperature dependence to different combinations of accepting modes. Reprinted with permission from reference 51.

predominantly produced by the SGE whereas the current along the perpendicular axis is mainly the result of the CPGE. A microscopic theory of the SGE for direct intersubband optical transitions has been developed and is in good agreement with these experimental findings (52). The results will be used to design samples with enhanced spin galvanic and Rashba effects, both of which are important for spintronic devices.

Biomolecules. The last example of relaxation phenomena involves investigations of the vibrational lifetimes of protein modes in the mid- and far-IR. In general, temperature transients are limiting for biological samples, and pulse slicing is often necessary for these experiments. Pump-probe experiments in the mid-IR measured the vibrational lifetime of the amide I mode in different systems ranging from the simple amino acid alanine and the almost entirely α-helix protein myoglobin to the predominantly β-sheet photoactive yellow protein (53). By pumping on the blue side of the amide I mode of myoglobin an unusually long, nonexponential excited state relaxation was observed that is neither present for alanine nor for photoactive yellow protein. These results suggest that the α-helix can support longer-lived nonlinear states. More recently, collective modes in proteins also have been investigated (54). These modes are considered to be essential for functionally important conformational transitions in proteins. Using the far-IR pump-probe beamline the low-frequency collective modes of bacteriorhodopsin, a transmembrane protein, have been excited at 87 μm. The observed transmission change depicted in Fig. 13 shows that these modes have an extremely long vibrational lifetime of more than 500 ps when compared with the higher frequency modes such as the amide I mode with a vibrational lifetime of only
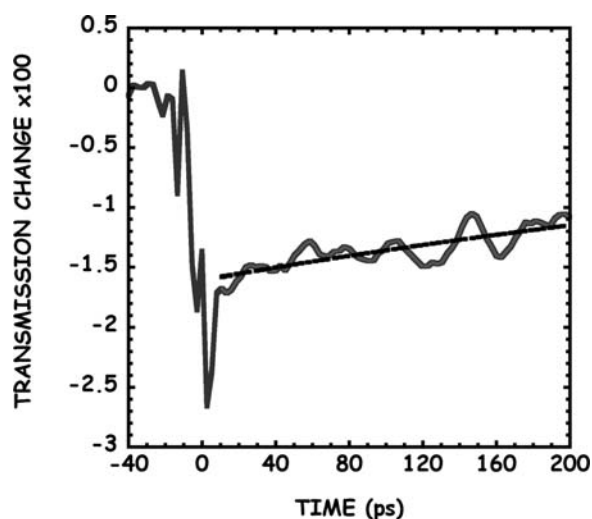
Figure 13. Pump-probe response of bacteriorhodopsin at 87 μm. The dotted line is a single exponential fit to the data with a time constant of 500 ± 100 ps. Reprinted with permission from reference 54.

Figure 14. The emission spectrum from a post-AGB object taken by the ISO satellite (upper trace, left axis) compared with the wavelength spectrum of TiC nanocrystal clusters recorded at FELIX (lower trace, right axis). Reprinted with permission from reference 57.

2 ps. The remarkable long lifetime of the far-IR vibrational excitation compared with the amide I mode may be related to the fact that fewer pathways for energy flow are available in the far-IR and to the relatively weak solvent damping with low hydration. The results suggest that there is a connection between the relatively slow anharmonic relaxation rate and the observed rate of conformational changes in a protein.

Gas-phase IR spectroscopy

Infrared resonance-enhanced multiphoton ionization (IR-REMPI) takes advantage of the tunability of the FEL and its high fluence on the microsecond timescale. Whereas the initial IR-REMPI experiments investigated fullerenes, the technique has been used to investigate (bio)molecules, clusters and complexes in the gas phase. A recent review on IR-REMPI studies can be found in von Helden *et al.* (55). In general, gas-phase spectroscopic experiments are characterized by (very) low absorption of the sample. Because the detection scheme is based on dissociation or ionization of the species, a strongly nonlinear dependence on the laser fluence is found and therefore FELIX typically operates in the 1 GHz-mode for this application.

Fullerenes. In the pioneering fullerene experiments, C_{60} molecules were excited to an internal energy of about 35–40 eV corresponding to 600 photons at the resonance frequency of 19.2 μm (56). At this internal energy, the C_{60} molecules can undergo thermionic emission of an electron, and the C_{60} ion can be detected very sensitively by mass spectrometry. Recording the mass spectrum of a species as a function of the FEL wavelength allows the measurement of the IR spectrum of the neutral molecule.

Nanocrystals. The breadth of research enabled by the IR-REMPI technique was nicely demonstrated when the IR spectra of gas-phase titanium carbide nanocrystals were measured in the laboratory and showed a prominent feature at 20.1 μm, which compares favorably with a similar feature in observed spectra of postasymptotic giant branch (post-AGB) stars (57). The IR spectra of titanium carbide clusters were measured by IR-REMPI with FELIX and provide evidence for the previously proposed metallo-
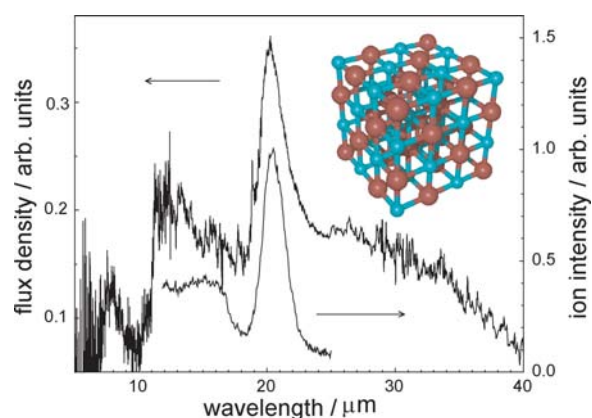
carbohedrenes (Met-Cars) structure of Ti_8C_{12} and nanocrystalline structure of $Ti_{13}C_{14}$ (58). Met-Cars are a unique class of stable clusters comprised of early transition metals bound to carbon in several unique stoichiometries corresponding to single cage-like structures as well as multiple cage structures. The similarity of the IR spectra of larger TiC clusters to that of $Ti_{13}C_{14}$ indicates that larger clusters have a nanocrystalline structure as well. The wavelength spectra of different sizes were therefore summed to a composite spectrum shown in Fig. 14, which has a strong peak at 20.1 μm and a width of about 1.8 μm. Most remarkably, the IR spectra of post-AGB objects are dominated by a distinct feature at 20.1 μm, which is present in the IR spectra of all sources at the same wavelength and with the same profile. The emission spectrum of the post-AGB object SAO 96709, taken by the Infrared Space Observatory (ISO) satellite is shown also in Fig. 14 for comparison. This 20.1-μm feature is unique to the post-AGB phase of the stellar evolution and has never been observed for objects in other evolutionary phases. These results have important implications for the understanding of the last stages of the evolution of low-mass stars and demonstrate a significant contribution of FELs to astrophysics.

Clusters and complexes. Whereas the IR-REMPI technique makes use of a change in the charge state, alternatively a change in the composition (infrared multiphoton dissociation, IR-MPD) of the species under study can be used for recording the IR spectra. The two examples for IR-MPD spectroscopy in a molecular beam apparatus discussed here—CO-rhodium (Rh) cluster complexes (59,60) and metal clusters (61)—demonstrate the necessity for broadband tunability from the mid-IR to the far-IR regions. The IR-MPD method requires that laser light is resonant with an IR-active mode of a cluster and that the cluster absorbs one or more photons. If this energy storage leads to dissociation of the complexes, their mass spectrometric intensity will be decreased. IR-depletion spectra are constructed by recording the ion intensities as a function of the FELIX wavelength.

The study of complexes of CO adsorbed on metal clusters is driven by the catalytic activity of transition metals dispersed on supports. The IR-MPD technique provides the sensitivity to study the IR spectra of a metal–CO complex in the gas phase without the influence of the support. The stretching frequency of CO is known to be highly sensitive to the structure and the electron density at the

binding site and therefore represents an excellent probe when studying structural changes as a function of, *e.g.*, the size or the charge state of the metal cluster. The IR spectra of neutral, cationic and anionic Rh_nCO complexes with n ranging from 3 to 15 were recorded in the frequency range of the CO-stretching vibration from 1650 to 2200 cm^{-1}. It was found that the adsorption site of the CO molecule strongly depends on the size and the charge of the cluster (59,60). A general picture of the binding of CO to gas-phase Rh clusters emerged, and two different regimes of CO binding depending on the cluster size could be identified. Clusters with $n \geq 5$ show predominantly binding of the CO molecule on top of a metal atom of the metal cluster. As the cluster size increases, one expects the properties of the charged species to converge to those of the neutral species and eventually to those of the bulk; this point has not been reached at $n = 15$. For the smaller clusters with $n \leq 4$, a much more dramatic dependence of the binding site on the cluster size and the cluster charge is found. These studies hold great promise for elucidating the chemistry of small clusters and therefore represent a key step toward more complex systems relevant for catalysis.

It was shown recently that IR-MPD can also be employed to investigate pure metal cluster complexes. The far-IR spectra of vanadium cluster cations are measured via the dissociation of a complex formed with argon for cluster sizes ranging from 6 to 23 in the frequency range from 150 to 450 cm^{-1} (61). The spectra shown in Fig. 15 are unique for each cluster size and therefore represent a true fingerprint of the cluster structure. The geometric structure of the clusters can be identified by comparison of the experimental IR spectra with model spectra obtained from density-functional theory (DFT) and thereby contribute to the fundamental understanding of the structures and properties of small metal cluster systems.

IR-MPD also is well suited to study complex systems in an ion trap. The IR spectra of a variety of systems were measured, *e.g.* the gas-phase spectrum of the protonated water dimer, $H_5O_2^+$ (62). Proton transfer through hydrogen bonds plays an important role in many (bio)chemical processes, but the detailed molecular mechanism is not yet established. In this experiment a sophisticated tandem mass spectrometer/ion trap setup has been connected to the FELIX beamline. The water cluster cations were produced in an ion-spray source, mass selected and accumulated in a linear RF ion trap at a temperature of about 100 K. The trapped ions were irradiated by a single macropulse and the dissociation product—in this case H_3O^+—was detected mass selectively while the wavelength was scanned over the range of the shared proton vibrations. Strong bands were observed in the range from 1600 to 1740 cm^{-1}. Comparison of the experimental spectrum with multidimensional quantum calculations shows the importance of intermode coupling in those shared proton systems.

Recently, another ion trap apparatus with extremely high mass resolution, a Fourier-transform ion-cyclotron mass spectrometer (FTICR-MS), was installed at FELIX in collaboration with the National High Magnetic Field Laboratory in Tallahassee, FL. This apparatus has proven to be a versatile tool for gas-phase spectroscopy of large (bio)molecules and clusters as well as for gas-phase synthesis of ions allowing for structural characterization of systems with significant chemical complexity. The IR-MPD spectrum of the Cr^+(aniline) complex recorded with this FTICR-MS is shown in Fig. 16, together with the calculated spectrum for two isomeric structures with the Cr^+ either bound to the ring or bound to the nitrogen (N) of the amino group. As the computed
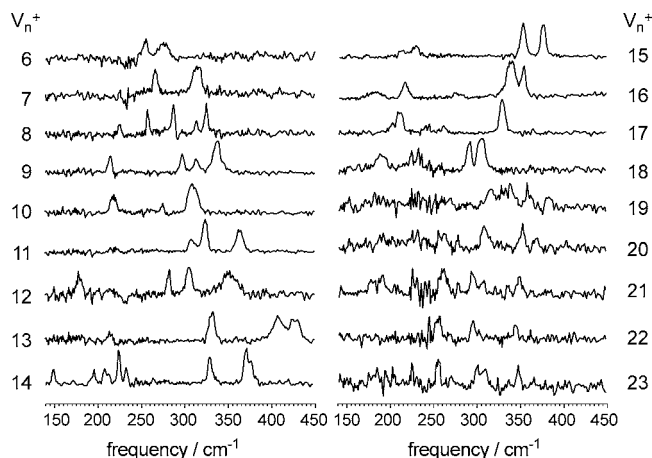

Figure 15. Far IR-MPD spectra of the argon complexes of vanadium cluster cations V_nAr^+ ($n = 6$–23) are measured in the range from 140 to 580 cm^{-1} (depicted only up to 450 cm^{-1}) (61).

binding energies for these structures are almost the same, experimental data were necessary to resolve this ambiguity—the Cr^+ binds to the ring of the aniline (63). Another example is studies probing the vibrations of shared OH+O bound protons in the gas phase that nicely build on the investigation of protonated water dimer discussed above. Here, the IR-MPD spectra of a number of gas-phase species with bridging protons were recorded (protonated dimethyl ether, protonated diethyl ether and protonated diglyme) and compared with model calculations (64). Given the similarity between the spectra measured in this study and the spectrum of the protonated water dimer (62), it seems reasonable to assume a general spectroscopic signature of a proton forming a strong hydrogen bond between two equivalent oxygen atoms.

Biomolecules. This final example of gas-phase spectroscopy at FELIX makes use of a change in quantum state to measure the IR spectrum of, *e.g.*, biomolecules such as amino acids, sugars and nucleobases (65–67). The method employed in these studies is called IR ion-dip spectroscopy (IR-IDS). The molecules under study are resonantly ionized by a pulsed UV laser tuned to the conformer-specific transition frequency to produce a constant ion signal. The IR laser, FELIX in this case, interacts shortly before the UV laser with the molecular beam. If the IR laser is resonantly exciting a vibrational transition, the ground state of the molecule is depleted, and as a result the UV ion signal decreases. Thus by monitoring the UV ion signal as a function of the FELIX wavelength, the IR spectrum is measured. Using IR-IDS the spectra of three different conformers of the amino acid tryptophan were measured in the frequency range between 300 and 1500 cm^{-1} and represent the first spectra of gas-phase biomolecules in the molecular fingerprint region (65). The spectra are depicted in Fig. 17 and show immediately that they are unique for each conformer, which indicates that the actual conformation has a large effect on the vibrational spectrum. Overall, the model spectra calculated using DFT methods (Fig. 17) match the experimental spectra well. The potential of the IR-IDS method to study larger molecules has been demonstrated by studies probing the glycosidic linkage of a lactoside (66) as well as measurements of the single and paired nucleobases guanine and cytosine (67). These results are encouraging for future studies on identification of conformational folding of larger molecules by means of their IR absorption characteristics.
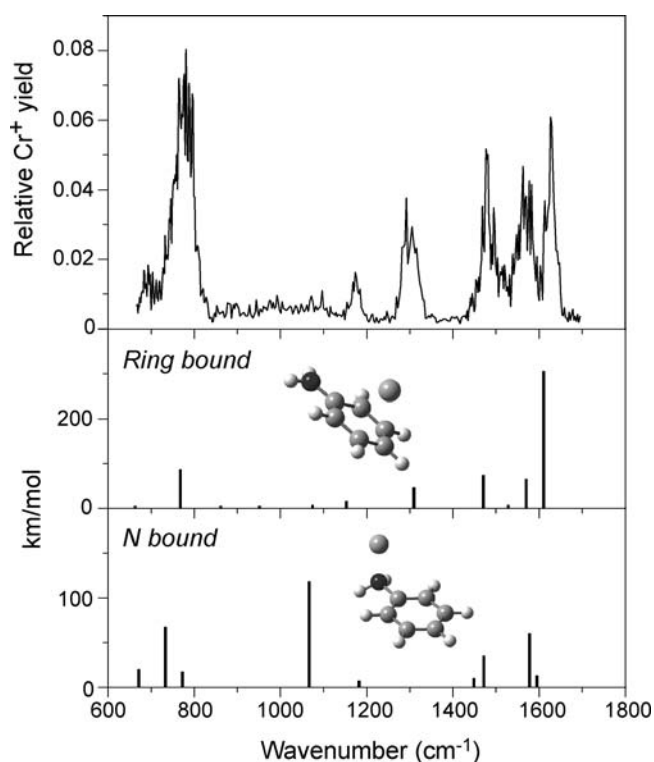
Figure 16. IR-MPD spectrum of the Cr^+(aniline) complex and the calculated IR spectra of the two isomeric structures with the Cr^+ bound to the aniline ring and bound to the nitrogen of the NH_2 group. The comparison shows that the complex is formed via binding to the ring. Reprinted with permission from reference 63.

Future enhancements of FELIX

The development of a third beamline is underway that will allow user experiments access to the much higher powers present within the FEL cavity (68). To date, the design phase has been finished and the construction of free-electron laser for intracavity experiments (FELICE) has begun; first lasing is expected in spring 2006. Two intracavity experiments are planned: a molecular beam apparatus and a high-resolution FTICR-MS. FELICE will cover the wavelength range from 3 to 100 μm and is expected to increase the power available to the intracavity experiments by a factor of 100 as compared with FELIX and thereby open up the field for new and exciting experiments particularly in molecular physics.

Summary of FELIX applications

These examples have shown that FELIX has been an essential tool for the measurement of vibrational relaxation processes in condensed matter and for gas-phase spectroscopy having a significant impact on applications research involving amorphous materials, spintronics, nanostructures and nanocrystals, biomolecules, fullerenes, clusters and complexes. The fields of research using IR-REMPI and IR-MPD have been expanding rapidly. Multiphoton IR excitation has a bright future for the spectroscopy of gas-phase (bio)molecules, clusters and complexes. At present, the wide tuning range and high pulse energies per microsecond make FELIX the laser of choice for these studies, and FELs most likely will continue to enjoy an advantage for these types of experiments relative to other light sources.

MATERIALS ANALYSIS AND PROCESSING USING AN IR MARK-III FEL

The Mark-III FEL combines broadly tunable (2–10 μm) picosecond pulses, high pulse repetition frequency and high peak power (69), making it an effective tool for laser ablation, organic materials synthesis and modification and even mass spectrometry. Because the output is in the mid-IR, the laser-material interaction with the Mark-III FEL is qualitatively distinct from femtosecond Ti:sapphire laser systems operating at 800 nm: the interaction with materials is marked by high local densities of vibrational, rather than electronic excitation. This has two advantages: first, the relative probability of complex electronic excitation (and photochemistry) is decreased, and second, the specific vibrational mode associated with the initial excitation is often well understood.

As the following examples illustrate, this new regime for materials analysis and processing complements that afforded by solid-state and gas-laser systems operating in the UV to near-IR spectral range. The three examples show respectively the opportunities created by (1) the exceptionally gentle ablation mechanism of the FEL; (2) the mid-IR tunability of the FEL; and
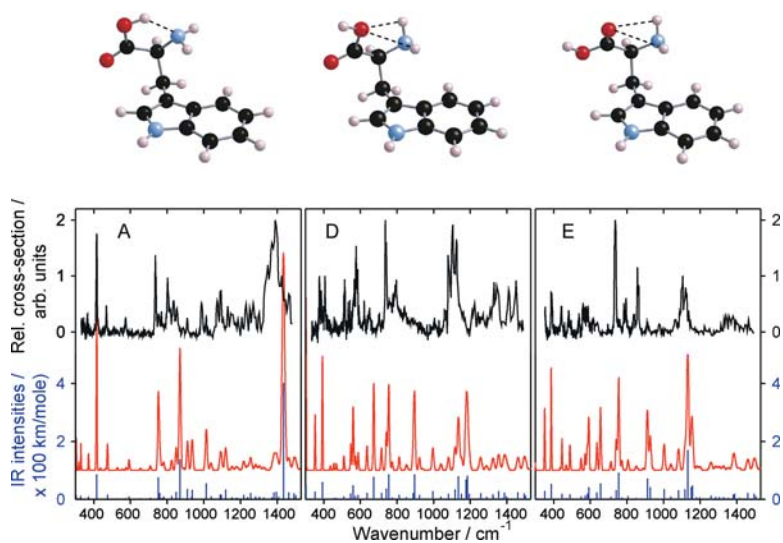

Figure 17. Infrared absorption spectra of three conformers of tryptophan displayed together with a theoretical spectrum. The corresponding geometries are shown above the spectra. Reprinted with permission from reference 65.

(3) the high pulse-repetition rate and high micropulse intensity combined with low micropulse fluence of FEL radiation. These examples also serve to benchmark the lasers that will extend these examples to tabletop laser systems and to other applications.

Two-color matrix-assisted laser desorption and ionization

One of the most important analytical techniques for characterizing large molecules is matrix-assisted laser desorption–ionization mass spectrometry (MALDI-MS). In conventional MALDI-MS, an analyte molecule was cocrystallized at low concentration in a weak organic acid with strong UV absorption. A nanosecond UV laser, typically the inexpensive N_2-gas laser, ablates a thin layer of material from the matrix. During the ablation process, a small fraction ($\sim 10^{-6}$) of the embedded analyte molecules would be ionized through a process that is widely believed to result from collisions in the laser plume between ion donors from the matrix and appropriate acceptors on the analyte molecule. This process of "soft ionization" was honored with the Nobel Prize for Chemistry in 2002.

It has long been known that MALDI with IR lasers broadens the class of possible matrix materials and leads to improved mass spectrometry of such diverse systems as: nucleic acids (70); phosphorylated, glycosylated or sulfated peptides (71,72); and proteins fixed in thick media such as polymer membranes (73). IR-MALDI at 2.94 μm clearly results in less fragmentation of large proteins and noncovalent complexes than UV-MALDI when using the same matrix (72,74,75). Using the FEL, direct IR laser desorption of biomolecules embedded in frozen aqueous solutions (76) and in polyacrylamide gels (77) has been demonstrated by selectively exciting vibrational modes of the ice or gel matrix.

Because of the large laser penetration depths of IR compared with UV, IR-MALDI at 2.94 μm ejects approximately 10^3 times more sample material per laser shot than UV-MALDI under typical conditions; the total ion yield is less than 10^{-6} of the ejected material (78). This can be an advantage in certain applications, and indeed, the greater quantity of ejected material is probably responsible for the higher ion yields of very large biomolecules in IR-MALDI. However, there is another way to capitalize on the large volume of neutrals ejected by an IR laser. In the following example, we use two lasers, an IR laser to ablate a substantial quantity of material without electronically exciting it, and then at an appropriate time in the expansion of the ablation plume, a UV laser to ionize the matrix molecules and thereby enhance the fraction of ions that enter the mass spectrometer. By setting the delay between the IR and UV laser pulses, it is possible to maximize the probability of charge transfer in the laser plume while minimizing the probability of subsequent collisional neutralization.

Figure 18 shows three MALDI mass spectra of immunoglobulin G (IgG, mass 166 kDa) in sinapinic acid. The UV (N_2, 337 nm) and IR (FEL, 5.9 μm) laser fluences were set to just above threshold, resulting in the spectra shown in the two lower traces (intensities have been increased 10× for these spectra). When both lasers were used, and the UV laser was delayed from 0 to 500 ns relative to the IR laser, the signal-to-noise ratio is enhanced by a factor of up to 50. The spectrum shown in the upper trace of Fig. 18 was taken with a 190-ns delay of the UV laser relative to the IR laser. The resulting two-color spectrum has many of the qualities of an IR-MALDI mass spectrum: multiply charged monomers and oligomers of the analyte are observed without peak broadening to
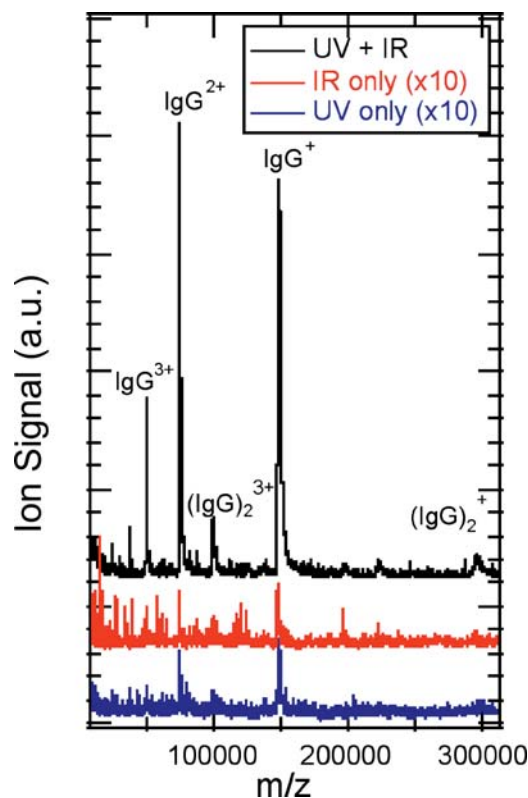

Figure 18. IR-MALDI mass spectra of a sample containing IgG (mass 150 kDa) ions in a 2,5-DHB matrix at an FEL wavelength set to 2.9 μm. The starting material is identical in each case. From bottom to top: Mass spectrum with a nitrogen laser (337 nm); mass spectrum with the FEL set to 2.94 μm; mass spectrum with the FEL set to 2.94 μm and the nitrogen laser at 337 nm. Delay between FEL and nitrogen laser pulses was set to 190 ns.

the low-mass side seen in UV-MALDI that indicates fragmentation (79). At the same time, these spectra exhibit the shot-to-shot reproducibility associated with UV-MALDI. The ability to independently vary fluences, delay times and the mass spectrometer ion optics also provides a means of analyzing separately the ablation and ionization processes thus opening new windows onto the mechanisms of ion formation in MALDI (80).

Mass spectrometry of complex environmental materials

The tunability of the FEL makes it possible to adapt MALDI-MS procedures to identify metal–ligand complexes in poorly characterized or contaminated samples. Small metal-organic molecules and especially carboxylic–alkali complexes are important in biological processes (81) such as cation transport through membranes (82,83); interface physics and chemistry (84); and mass spectrometry (85–87). In fact, metal ions are sometimes added to compounds containing no acidic or basic groups such as polymers (88) and carbohydrates (89) to increase ion yield. However, alkali atoms such as potassium and sodium—ubiquitous especially in biological systems—tend to suppress positive ion signals in MALDI (90,91) and by forming multiple alkali adduct peaks, reduce signal-to-noise ratio and broaden spectral lines (92,93).

One of many current challenges in environmental mass spectrometry is posed by hundreds of millions of liters of mixed chemical, radioactive and flammable wastes stored primarily in
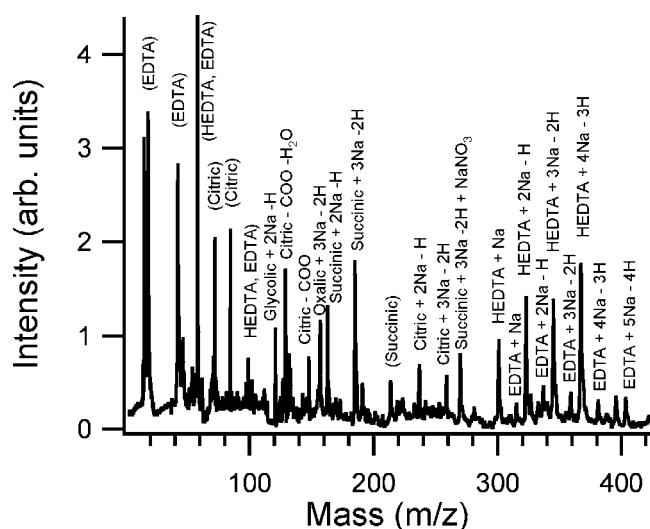
Figure 19. IR-MALDI mass spectrum of a tank waste simulant mixture containing HEDTA, EDTA, succinic, citric, glycolic and oxalic acids in the proportions described in the text. The mass peaks are clearly identified including those with sodium adducts. Sodium ion and sodium-ion cluster peaks have been deleted from the spectrum for clarity.

enormous carbon-steel, underground tanks at U.S. Department of Energy sites. Large quantities of chelants–including ethylenediaminetetraacetic acid (EDTA), hydroxyethyl ethylenediamine triacetic acid (HEDTA) and citric acid, nitrates and nitrites were originally added to the hazardous waste products to reduce acidity and preserve tank integrity. However, the long storage time has resulted in leaks in the tanks. Moreover, in the evolving tank environment, condensed-phase reactions between these organic chelators (fuel) and nitrate/nitrite salts (oxidizers) could lead to explosive release of radionuclides and toxic materials to the environment (94).

Fortunately, as the tank waste ages, chemical and radiolytic degradation of the chelators into smaller compounds reduces the organic fraction available as fuel. Hence, the relative abundance of organics in the tank wastes indicates the extent of degradation, making quantitative analysis a critical priority. Mass spectrometric analysis improves the speed and accuracy of the risk assessment required before waste treatment or relocation. However, the harsh chemical and radioactive environment and presence of large amounts of sodium complicates MALDI-MS analyses of the organic content. Unlike previous MALDI studies of tank waste simulants using exogenous matrices (90,95), we used sodium nitrate, an intrinsic component of the waste composite, as the matrix and tuned the FEL to match one of its vibrational absorption modes. This eliminated the need for an exogenous matrix whose mass signature might obscure the relatively low-mass analyte ions as well as complicate matrix-analyte chemistry in UV-MALDI (96,97).

With IR-MALDI, tuning the laser to the ν_2–ν_4 C=O stretching vibration of the sodium nitrate at 7.1 μm, it was possible to identify all of the organic species in tank waste simulants as shown in Fig. 19 (96). In addition, the studies showed that the ion spectra are strongly dependent on the specific ablation wavelength used to cause ablation; the ions are formed by gas-phase collisional processes; and the memory of any cation complexes characteristic of the solid state is lost. Because of the simple structures of the

molecules involved, it was even possible to make reasonable conjectures about the specific binding sites of the sodium ions and the effect of ionization on the structure of the ion complexes observed, conclusions qualitatively confirmed by computational modeling. Importantly, because the initial laser excitation targeted only specific vibrational modes, these conclusions about the ionization mechanism remove the ambiguities that arise from laser-induced photochemistry during ablation and MALDI with fixed-frequency UV lasers.

IR matrix-assisted pulsed laser evaporation of nucleotides

The two-laser MALDI experiment discussed above provides compelling evidence for the copious ejection of intact, neutral biomolecules by the Mark-III FEL. This suggests a novel deposition technique for transferring intact biomolecules in the gas phase: IR matrix-assisted pulsed-laser evaporation (IR-MAPLE). IR-MAPLE is closely related, of course, to IR-MALDI; the emphasis in IR-MAPLE, however, is on generating gas-phase biomolecular and other organic ions so that they can be deposited on surfaces such as cantilever sensor structures.

In the common techniques for growing thin films of inorganics—such as pulsed-laser deposition (PLD), molecular beam epitaxy (MBE), physical and chemical vapor deposition (PVD, CVD)—a stream of energetic atoms or molecules is deposited on a clean surface under high-vacuum or ultrahigh-vacuum (UHV) conditions. To avoid thermal damage, thin films of organic or polymeric materials are instead deposited by solvent-based techniques such as solution casting, dip coating, spin coating and aerosol transfer. Higher densities of certain materials can be attached to certain metal surfaces, such as gold, by self-assembly (98); however, it is often difficult to effectively coat micro-electromechanical device structures by such means (99).

A number of applications, ranging from sensors to optoelectronics, would benefit from a vacuum-deposition technique for organic macromolecules. We have drawn on the same reservoir of biologically benign matrix materials that selectively absorb mid-IR radiation to develop an analog to UV-MAPLE (100) that avoids both the complex photochemistry and the freezing of the biomolecules in highly aromatic matrices. In one early experiment (101), a solution of a standard biotinylated-protein mixture (Bio-Rad, Hercules, CA, Catalog Number 161-0319) in water, including bovine serum albumin (BSA, mass ~166 kDa), was frozen in liquid nitrogen before insertion into the vacuum chamber. A thin film of the labeled BSA was transferred by resonant-laser evaporation of the ice at 2.94 μm onto a nitrocellulose-coated glass slide through a gold shadow mask. After deposition, the slide was washed with a blocking protein and then tagged with a site-specific fluorescent streptavidin label. Images of the fluorescence from the structured film indicated successful transfer and preservation of the site-selective biological activity in the deposited proteins.

DNA can also be effectively transferred to a metal, semiconductor or insulator substrate by the IR-MAPLE technique as summarized in Fig. 20. Frozen solutions of two different kinds of DNA in water ice were used as the target, which was subsequently irradiated by 2.94-μm light from the FEL, corresponding to the O–H stretch vibration of water. Electrophoresis of the transferred material indicated that the DNA underwent virtually no fragmentation in the regime of moderate macropulse doses. Interestingly, however, it proved impossible to transfer DNA successfully using

an erbium yttrium-aluminum-garnet (Er:YAG) laser at similar fluence levels, possibly indicating a role for ultrashort pulse duration—*i.e.* high intensity but low fluence—in the ablation process. This intensity dependence suggests that the denaturation of the DNA is a direct result of the thermal loading experienced during the laser-induced transfer process using nanosecond pulses. In that sense, the energy budget is a sensitive thermometer for the transport mechanism.

The transport of the globular salmon-sperm DNA is not a particularly severe test of the IR-MAPLE technique because it has a rather broad mass distribution and is somewhat insensitive to fragmentation during ablation. The second electrophoresis trace is thus the more interesting one, showing the successful IR-MAPLE transfer of pBluescript DNA, which has two distinct forms: one a circular DNA fragment, the other supercoiled. (It is a standard used by molecular biologists as a calibration marker.) In the lower panel of Fig. 20, the bands of the sample as received and the sample from the transferred film are shown. The fact that the mass distributions are identical indicates that the DNA has been transferred intact from the ice matrix to the film plate. To test for functionality, a fluorescent protein that can be expressed by the DNA would have to be used following deposition.

This result demonstrates the potential for thickness-controlled, conformal transfer of nucleic acids and proteins to microstructured or even nanostructured sensors for use in biological and chemical detection schemes, in much the same way as functionalized polymers have already been transferred by resonant-IR pulsed-laser deposition (102).

Summary of Mark-III FEL materials analysis and processing applications

These three examples illustrate the power of the Mark-III FEL as a tool in the analysis and processing of organic materials. Indeed, particularly in the second case, the FEL is the paradigmatic example of a materials-processing regime first described theoretically a few years ago (103) and so far realized in practice only with the Mark-III FEL. It remains to be seen whether or not solid-state laser systems can duplicate the combination of high peak and average powers, high intensity and low fluence seen in operating FELs. Picosecond and femtosecond optical parametric amplifier systems can produce tunable, mid-IR micropulses with energies comparable to those of the Mark-III FEL; however, at present kHz repetition frequencies, such lasers do not have the average power needed for materials processing. Nevertheless, ultrasensitive mass spectrometry with these lasers is a definite possibility at present. Moreover, with schemes already in the breadboard stage for solid-state lasers that can reach into the mid-IR, the possibility of tabletop laser materials processing and analysis in the mid-IR may well be realized in a few years (104).

BIOPHYSICAL AND BIOMEDICAL RESEARCH USING AN IR MARK-III FEL

The ablative properties of the Mark-III FEL have biomedical applications in addition to the analytical and processing applications described in the previous section. A series of biophysical experiments first demonstrated that tuning to wavelengths near 6.45 μm results in *in vitro* tissue ablation with minimal and, at times, undetectable collateral damage in neural tissues (105). Similar *in vitro* results were seen for ocular and dermal tissues. The surgical advantage of such laser incisions was apparent and
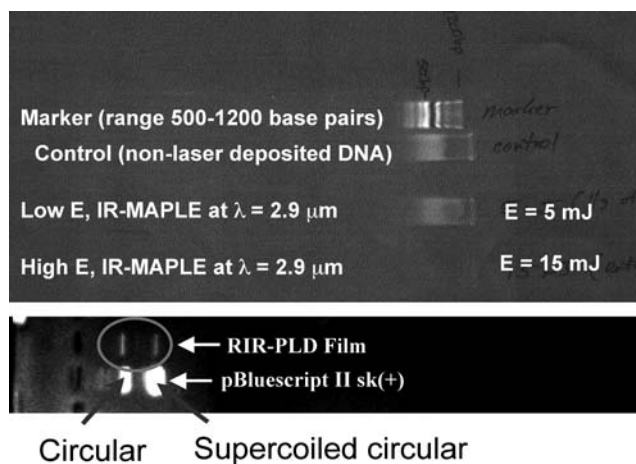

Figure 20. Electrophoresis traces of nucleotides deposited by IR-MAPLE from a water–ice matrix. Top trace, top to bottom, salmon-sperm DNA, marker shows range from 500 to 1200 base pairs; control trace using nonlaser-deposited DNA; trace of IR-MAPLE–deposited material at an FEL wavelength of 2.9 μm, macropulse energy 5 mJ; trace of IR-MAPLE–deposited material at the same wavelength but with macropulse energy 15 mJ. Note the complete absence of an electrophoresis band in the range of masses appropriate to salmon-sperm DNA. Bottom trace, top to bottom, IR-MAPLE–deposited film of pBluescript II sk(+) DNA at FEL wavelength of 2.9 μm; electrophoresis trace of pBluescript starting material. Reprinted with permission from reference 101.

motivated additional research to explore the possibility of bringing this FEL-based capability to human surgical care. This required (1) an extensive series of *in vivo* animal studies to confirm that the advantageous ablation results still held; (2) the construction of human surgical suites within access to a Mark-III FEL; (3) the upgrade of the FEL to meet the reliability and performance requirements of a medical laser; (4) the development of beam-delivery systems for human surgery; and (5) regulatory approval. *In vivo* animal experiments confirmed previous *in vitro* results, and the research progressed to successful human surgery. A review of the biophysical, biomedical and bioengineering research that supported successful human surgical applications as well as the upgrade of the Mark-III FEL to qualify as a medical laser for human surgery have been published recently (69,106). We review parallel research questions related to the mechanism governing IR tissue ablation, the application of these results to specify the operating parameters for a surgical laser based on conventional laser technology and briefly summarize surgical applications.

Photophysical mechanisms

FEL tissue ablation takes advantage of the specificity of the mid-IR "fingerprint region" of the vibrational spectrum (105). The spectral features in the 2 to 10 μm regime can be measured in the condensed phase at native hydration with FTIR spectroscopy as shown in Fig. 21. The spectral features correspond to localized vibrations. Many soft tissues are well approximated as ~75% water and ~25% nonaqueous components. Water in the condensed phase can absorb IR radiation via the bending mode near 6.1 μm and many proteins can absorb IR radiation via the amide I and amide II vibrational modes centered at 6.00 μm (1665 cm^{-1}) and 6.45 μm (1550 cm^{-1}), respectively. These three spectral features form a partially resolved band where each is likely to be subject to inhomogeneous line broadening. The Mark-III FEL is tunable from
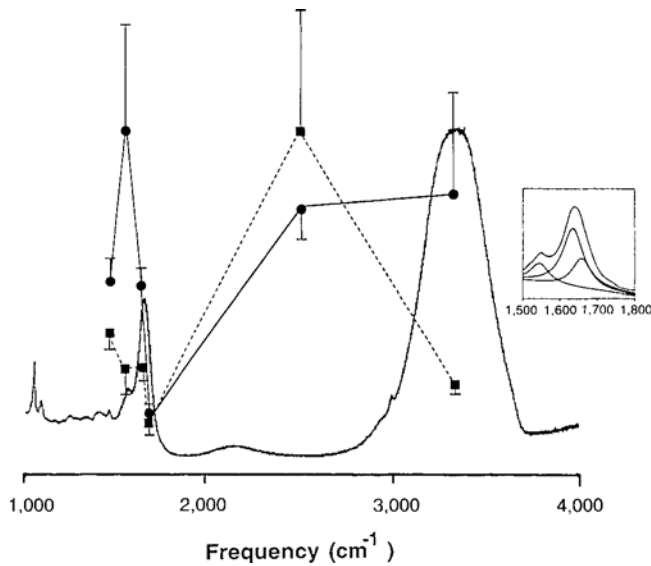
Figure 21. Relative ablation yield (circles) and collateral damage (squares) plotted against the Fourier-transform infrared spectrum of corneal stroma taken with an attenuated total reflectance sample cell. Spectral curve fitting results are displayed in the inset. Reprinted with permission from reference 105.

2–10 μm and as such can be tuned within this unresolved band to excite simultaneously both the vibrational modes of protein and the bending mode of tissue water. In addition, the high average power of the Mark-III FEL results in substantial ablation rates. Interestingly, the eigenfrequencies for these three modes are relatively insensitive to the type of soft tissue, and this strategy for simultaneously targeting protein and water with wavelengths near 6.45 μm radiation applies to soft tissues in general.

The mechanism responsible for the advantageous ablative properties of the Mark-III FEL has been investigated in terms of pulse structure in addition to wavelength. The Mark-III FEL has a complex pulse structure with high peak power in addition to high average power. A micropulse is about a picosecond in duration with tens of microjoules in energy. A burst of tens of thousands of micropulses, at a repetition rate of 3 GHz, comprises a macropulse. The duration of the macropulse is about 5 μs with a total energy of tens of millijoules. The repetition rate of the macropulse can be up to 30 Hz. A series of investigations were carried out to determine the role of these pulse parameters in mid-IR tissue ablation. Importantly, a single Mark-III FEL macropulse can ablate tissue, reducing the investigation to picosecond, 350 ps and 2–6 μs content. Experiments demonstrate that ablation is not solely attributable to picosecond pulses so dynamics at longer timescales were considered. There is considerable experimental and theoretical evidence that the critical dynamics occur on the 1 to 10 ns timescales (107,108). The theoretical model is based on thermodynamics and chemical kinetics as applied to corneal stroma where the protein is predominantly collagen. According to this model, the absorption of 6.45-μm radiation heats the tissue water near the air–tissue interface to many hundreds of degrees in several nanoseconds due to the high average power of the FEL, as summarized in Fig. 22. At this heating rate, the outer saline layer reaches the superheat limit and then explosively vaporizes. Simultaneously, 6.45 μm radiation heats the collagen, driving the collagen–gelatin transition. Whereas collagen is ductile, denatured gelatin is brittle. Apparently the key to the ablative mechanism is differential
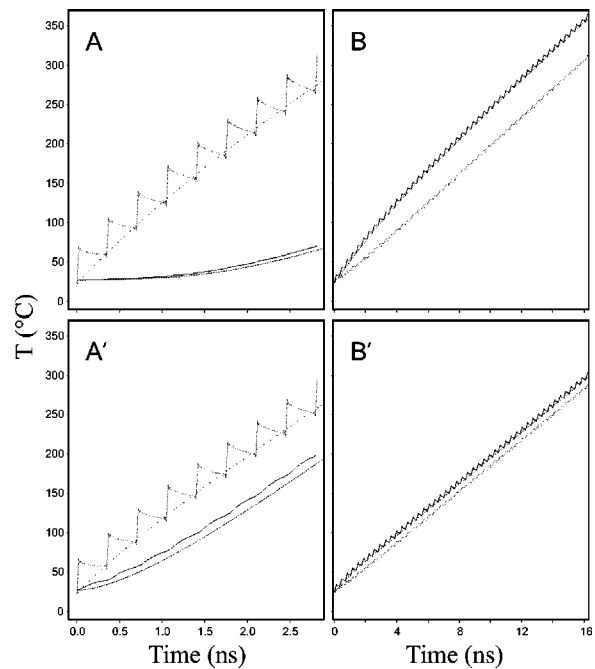

Figure 22. Thermal response to a pulse train. Surface layers exposed to A: 3.00 μm and B: 6.45 μm radiation. Layers 200 nm below the surface exposed to A′: 3.00 μm and B′: 6.45 μm radiation. In addition, the temperature response due to the Mark-III FEL pulse structure, protein (solid) and water (dotted), is compared with a 16.2-ns pulse with the same average energy, protein (dashed) and water (dot dash). The initial temperature was 25°C. Reprinted with permission from reference 107.

heating rates for the protein and water leading to brittle fracture at the onset of explosive vaporization, which results in the confinement of collateral tissue damage. The extent that the ductile–brittle transition precedes vaporization or vice versa depends on wavelength and determines whether there is an onset of significant collateral damage. The model was tested successfully with experimental observations at 6.45 μm and 3.00 μm, where in the latter case the absorption is dominated by the OH-stretch mode of water. The model attributes a significantly larger fraction of collagen denaturation at 6.45 μm relative to 3.00 μm, consistent with the experimental observation (105,109).

This theoretical analysis can also assess the consequences of varying the pulse structure and predicts how to relax the complex pulse structure of the Mark-III FEL and still maintain the experimentally observed preferential ablative properties (107,108). The dynamics for the ablative mechanism are the result of the thermodynamics and chemical kinetics of tissue and not imposed on the tissue by the pulse structure of the FEL. The differential heating rates must have the following characteristics: the rate must be fast enough to superheat the tissue water and the differential heating rates must drive a temperature separation between protein and tissue water, as observed in Fig. 22B, such that brittle fracture characterizes the onset of explosive vaporization. This analysis leads to the prediction that the micropulse duration can be extended from picoseconds to tens of nanoseconds and, as long as the average power is maintained, this should lead to similar ablative results.

Human surgical applications

The applications of the FEL to human neurosurgery and ophthalmic surgery were safe and successful (106,109,110). In

the neurosurgical cases, the tumors were exposed and the IR beam was delivered though a handheld wand. In the ophthalmic cases, the IR beam was delivered endoscopically through a 250 μm hollow waveguide, and surgery was performed on the optic nerve sheath. Currently, biomedical scientists are investigating FEL-based treatments for epilepsy and nerve repair following trauma.

The Mark-III FEL occupies a niche among medical lasers. The visible argon-ion laser can be transmitted through the structures of the eye and has been used to treat ocular tissues but is not effective at ablating tissue. The UV excimer is in routine use to ablate cornea; however, concerns about untoward side effects of UV photochemistry have restricted the application of UV lasers to nonnucleated tissues. The IR carbon dioxide (CO_2) laser also is in routine medical use, where a veneer of collateral damage can be advantageous to control bleeding. Many potential laser medical applications, however, are precluded by this zone of collateral damage.

The promise of IR laser tissue ablation lies in eloquent surgery near vital structures. Neurosurgical image-guided systems currently offer submillimeter accuracy, and automated laser systems for tissue resection are under active consideration by the neurosurgical community. Endoscopic laser delivery and diagnostic techniques along with image-guided systems (106) are particularly promising. Acceptance by the greater medical community, however, likely will necessitate more compact lasers that require fewer resources.

Current and future research

The relaxation of the micropulse duration from picoseconds to tens of nanoseconds admits several conventional laser technologies as potential IR medical lasers. The Mark-III FEL produces both high peak and high average power via a complex pulse structure that has not been reproduced by conventional lasers. However, a 10 ns laser with average power comparable to that of the Mark-III FEL and operating near 6.45 μm should be attainable using conventional laser technology.

Fracture due to substantial heating rates and at extreme temperatures is poorly understood. At the core of the dynamic model for IR tissue ablation is the ductile–brittle transition for protein. Collagen is a large, triple-helical molecule that clearly cannot fully denature into a random coil in tens of nanoseconds. Additional research, *e.g.* exploring the analogy between the superheating of water and the onset of polymer fracture or the fracture of interpolymer linkages, is necessary to understand the onset of brittle fracture at these short timescales in localized regions of tissue.

Summary of Mark-III FEL surgical applications

Surgical applications of the FEL rely on the inhomogeneous buildup of heat that supports a controlled degradation of material. High peak power, high average power and ease of tuning the wavelength of the Mark-III FEL were key to this research. Analogous control of degradative processes, *i.e.* an exceptionally gentle ablative mechanism, characterizes the mass spectrometry research summarized in the previous section.

UV FEL PHOTOEMISSION ELECTRON MICROSCOPY FOR NANOSCALE DYNAMICS

Real-time imaging of nanoscale dynamical processes with the ability to measure the electronic properties of surface structures with nanoscale resolution is an essential capability for nanotechnology.

The technique of photoemission electron microscopy (PEEM), which involves imaging photoelectrons excited from a sample surface, exhibits just these desired capabilities. The photoelectric effect requires intense excitation with light with photon energies near the threshold for photoemission, which is between 3–7 eV for most materials. The OK-4 storage ring FEL at Duke University is an ideal excitation source for this application (111).

The UV FEL provides two modes of operation: spontaneous emission and coherent lasing mode. The spontaneous radiation is continuously tunable from 4 to 7 eV, has a linewidth of <0.1 eV and delivers an average power of >3 mW to the microscope. The lasing mode is tunable over a range of 3.0 to 6.3 eV, depending on the installed cavity mirrors. For any set of mirrors, the tuning range ($\Delta E/E$) is approximately $\pm 8\%$ of the central energy. The lasing mode, with an average power of >15 mW and a linewidth of ~0.01 eV, is particularly appropriate for PEEM measurements of electronic properties of nanostructures. High surface sensitivity is achieved because the photoelectrons originate from electronic states near the surface. The system employed in our studies is a custom-designed third-generation PEEM obtained from Elmitech (Rungis, France). Shown in Fig. 23 are excitations that are important for this research. It is evident that through appropriate choice of photon energies (1) metallic regions on the surface can be identified; (2) semiconductors with different band gaps or strain can be distinguished; (3) regions with a high density of surface states can be imaged; and (4) many processes, which change surface work function or electron affinity, can be monitored. Therefore, by tuning the FEL to the appropriate wavelength, the PEEM images can be tuned for maximum contrast of the specific nanostructures on the surface. Moreover, the excited electrons have a small energy spread enabling imaging at the limits of the electron optics (*i.e.* <10 nm resolution).

Here we summarize three examples of applications of the UV-FEL PEEM. The first example presents results of nanostructure growth processes on Si surfaces where a new phenomenon was observed that was not anticipated in the extensive theoretical treatments on growth dynamics (112). The second example presents results of a study of the electronic properties of gallium nitride (GaN), which is a polar semiconducting material, surfaces (113). This research established a fundamental difference of the electronic band structure that is strongly influenced by the surface termination and the crystal polarity. The third example is a study of the electronic properties of individual melanosomes, an important biomolecule (114). This study of biological materials presents insight into the relation of chemical reactivity and melanosome type.

Dynamics of nanoscale island formation

In the ever-evolving science of microelectronics, the size of electronic devices is constantly decreasing. At present, Si-based metal-oxide-semiconductor (MOS) transistors are the device elements for the existing technology, which is based on lithographic patterning. The reduction in device dimension brings with it new challenges in nanometer-scale material processing and also opportunities for novel device structures. The evolution and subsequent coarsening of island structures on a surface are of crucial importance for controlling the fabrication of novel nanometer-scale structures and for fundamental understanding of thin-film growth processes (115). Moreover, self-assembly or self-organization of nanoislands and nanowires is a bottom-up approach that may replace some traditional (top down) lithographic
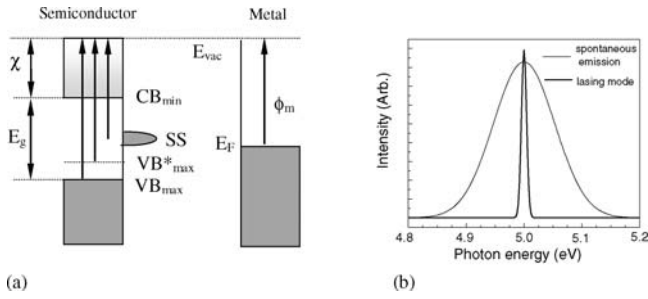
Figure 23. a: A schematic of the photo excitations from the surfaces of interest. The arrows indicate the photon energy to excite an electron above the vacuum level (E_{vac}). From the left to right the arrows represent excitation from the unstrained valence band maximum (VB_{max}), the strained $VB*_{max}$, surface states (SS) and a metallic region on the surface. b: The spectral output of the FEL in spontaneous emission and lasing mode with output centered at a photon energy of 5.0 eV.

Figure 24. A time sequence of PEEM images of a pair of TiSi$_2$ islands obtained with the sample at 1150°C: for a: 0 min, b: 4 min, c: 6 min, and d: 8 min, respectively. Images are 2 μm × 2 μm. Reprinted with permission from reference 112.

steps. Nanoislands have demonstrated single electron effects where the coulomb potential due to a single extra electron can strongly suppress the current through the nanoisland (termed the ''coulomb blockade''), and nanowires may exhibit ballistic transport and chemical sensitivity.

Titanium silicide formation can occur through a solid-state reaction of Ti on a Si surface. According to the binary phase diagram, titanium silicide (TiSi$_2$) is in chemical equilibrium with Si up to the melting point of Si. Research has established that TiSi$_2$ nanoislands are epitaxial with the Si substrate, indicating that strain can play a role in the energetics.

Island coarsening on surfaces involves the dynamics of material transfer and the kinetics of island growth. In an evolving surface, initially nucleated islands grow through the interactions between the islands (116,117). In postdeposition conditions, where no additional material is being deposited, Ostwald ripening (OR) is considered the primary coarsening mechanism for island growth (116,117). In OR, immobile larger islands grow at the expense of smaller islands through atom exchange between the islands. The driving force for OR is the adatom concentration difference between islands of different size (118,119). In contrast, we have observed distinctive island migration and coalescence for TiSi$_2$ epitaxial islands on Si surfaces: the coalescence of islands was not the result of random island motion but the result of directed island migration toward each other. As shown in Fig. 24, two TiSi$_2$ islands move attractively and subsequently coalesce during a time span of approximately 8 min at 1150°C (112). We note that observation of this type of an interaction is only possible with *in situ* real-time imaging.

Our proposed mechanism for attractive migration and coalescence is the growth–decay flow of the island edges because of a nonuniform concentration of drifting adatoms around the island (112). A dynamic equilibrium will be established between the islands and the diffusing surface atoms, and the net flux of atoms diffusing at the edges of an island will depend on the surrounding environment of the island. As a result, when two islands of similar size are formed in relative proximity to one other, a nonuniform concentration develops around each island, and the inner-facing edges have a higher probability of capturing adatoms emitted from each island than the outer-facing edges. The facing edges of the islands will grow through adsorption of Ti flux between the islands whereas the outer boundaries will shrink via Ti out-diffusion. The spontaneous growth–decay flow of the island edges leads to movement of the island's center of mass toward each other and subsequent coalescence.
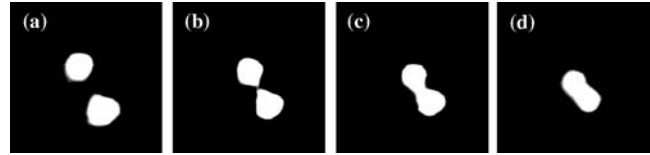
Electronic states of polar GaN surfaces

Optoelectronic devices based on wide bandgap GaN materials have led to high-power light emitting diodes with blue wavelength, which are now widely evident in large bright displays, signal lights and signs and potentially solid-state lighting. In our PEEM studies, a GaN film with laterally patterned Ga- and N-face polarities was explored (113). Wurtzite GaN has a spontaneous polarization where the polar axis is parallel to the c-direction of the crystal lattice. The orientation of the spontaneous polarization and the induced bound charges are determined by the film polarity (Ga or N-face). The Ga-face surface exhibits a negative bound charge, and the N-face surface exhibits a positive bound charge. The screening of these bound charges gives rise to surface band bending. We have established how these effects are manifested in PEEM images of GaN films with different local polarities.

A GaN film with laterally patterned Ga- and N-face polarities was fabricated using plasma-induced molecular beam epitaxy (PIMBE) (120). To explore the electronic properties of the different regions, we obtained PEEM images with photon energies from 4.5 to 6.3 eV in steps of 0.1 eV (Fig. 25). For photon energies below 4.8 eV, contrast between the two regions was not detected (Fig. 25a). However, for photon energies greater than 4.9 eV, emission from the N-face regions was observed, which led to a distinct emission contrast between the two domains (Fig. 25b). As the photon energy was increased from 4.8 eV, the emission from the N-face regions also increased leading to enhanced contrast (Fig. 25c). However, at 6.3 eV, the emission from the Ga-face region became more significant, and the emission contrast was relatively reduced (Fig. 25d). From these results, we can deduce that the photothreshold of the N-face region is less than ~4.9 eV whereas that of the Ga-face regions is greater than 6.3 eV.

To explain the much lower photothreshold at the N-face surface, we considered the effect of the polarity on the band structure at each surface. In n-type GaN, the energy-band diagrams for the Ga- and N-face surfaces are illustrated in Fig. 26. The bulk Fermi-level position of our GaN film was estimated to be ~0.05 eV below the conduction band edge for both Ga- and N-face regions. For the Ga-face region, the spontaneous polarization (−0.034 C/m^2) points from the surface to the substrate, inducing a negative bound charge at the GaN surface ($\sigma/e = -2.12 \times 10^{13}$ cm^{-2}). The negative bound charge at the surface is screened by the positively ionized donors close to the surface. This leads to upward band bending and a depletion region at the Ga-face surface (Fig. 26a). In contrast, downward band bending should occur at the N-face surface because of the opposite direction of the spontaneous polarization. The positive bound surface charge gives rise to a free electron accumulation layer at the N-face surface, fixing the Fermi level close to the conduction band edge. This accumulation layer leads to a slight downward bending of the conduction band edge at the N-face surface (Fig. 26b).
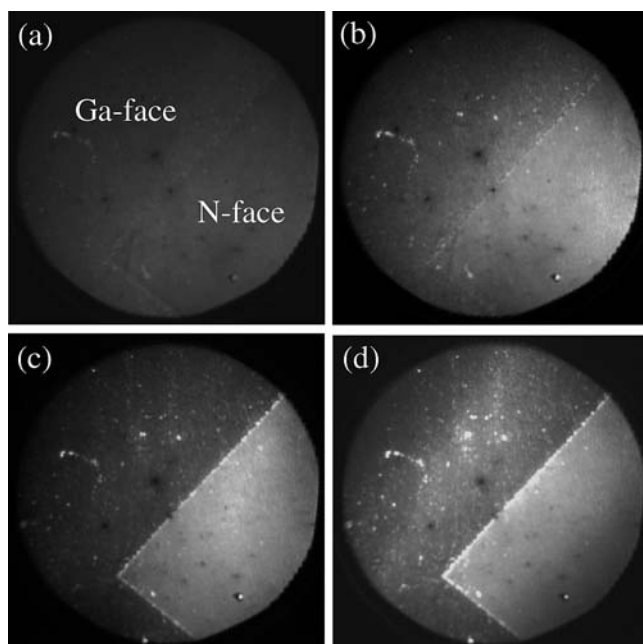
Figure 25. PEEM images a clean GaN lateral-polarity heterostructure. The Ga- and N-face regions are indicated and images were obtained with photon energies of a: 4.8 eV, b: 4.9 eV, c: 5.6 eV, and d: 6.3 eV, respectively. The field of view is 150 μm. Reprinted with permission from reference 113.

Figure 26. Energy band diagrams for a: Ga-face, and b: N-face GaN. The quantities χ_s, ϕ, and E_{th} are the surface electron affinity, work function, and photothreshold, respectively. The arrows represent the directions of spontaneous polarization, P_{sp} and the internal electric field E. Reprinted with permission from reference 113.

We suggest that the surface band bending gives rise to a variation in the photothreshold at the different polar surfaces. For upward band bending of the Ga-face region, the photothreshold at the surface is $\chi_s + E_g$ (Fig. 26a), and the electrons are photoemitted from the valence band edge for a photon energy greater than $\chi_s + E_g$. On the other hand, for downward band bending of the N-face region, an electron accumulation layer results because the conduction band minimum is slightly below the Fermi level. As a result, the electrons in the accumulation layer can be photo-emitted from the conduction band, and the photothreshold at the surface would be essentially the electron affinity (Fig. 26b). Thus, the relatively bright intensity at the N-face regions is attributed to electron emission from the conduction band because of downward band bending. Therefore, the polarity-dependent photothreshold causes a photoelectric yield difference between the Ga- and N-face regions and leads to the polarity contrast in the PEEM images of the GaN film (113).

Photoionization threshold of melanosomes

In studying biological samples, PEEM can be applied in two different yet complementary ways. First, PEEM can be used solely for imaging to obtain high contrast between features of interest in the image. PEEM imaging was applied to biological samples as early as 1972 (121). Since then, viruses and DNA (122), eukaryotic cells (123), cultured cancer cells (124) and cytoskeletons (125) have been studied. Because PEEM is a UHV technique, the samples must be fixed, and little if any water remains. Second, quantitative information on the electronic properties of the sample can be obtained. Photoemission quantum yield of several classes of biomolecules have been explored using PEEM (126,127). With a tunable light source, threshold photoionization energies can be determined. In the case in which the biological sample contains a rich spatial structure, it is possible that the threshold ionization
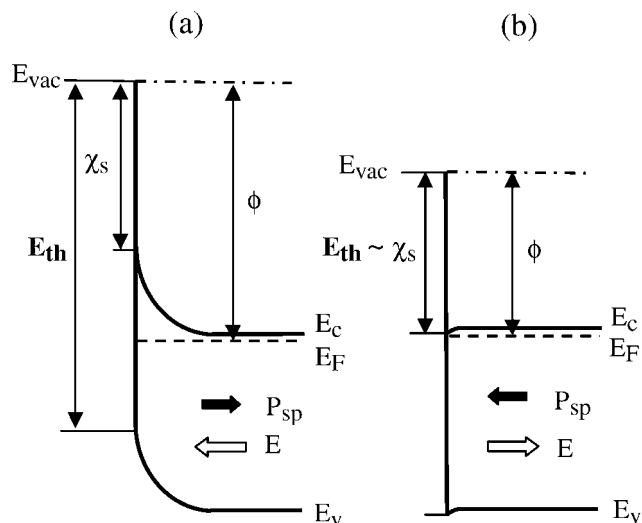
energy differs for the various constituents, and therefore, wavelength-dependent PEEM images will provide both imaging information as well as variation in the chemical properties (ionization potential) within the imaged region.

We have used PEEM to study unstained human eumelanosomes isolated from black hair and bovine eye retinal pigment epithelium (RPE) (114). Eumelanosomes are responsible for tissue pigment and in the RPE, eumelanosomes mitigate oxidative stress. It has been proposed that eumelanosomes serve a protective role and are involved with the onset of disease in neural tissues. Eumelano-somes do not require any fixation, dehydration, freezing or staining to study by electron microscopy (128). Films were prepared by spreading the suspension of extracted eumelanosomes in nano-pure water over the freshly cleaned Si-wafer surface and air-drying for <1 h.

PEEM images of assemblies of eumelanosomes were obtained at a field of view of 150 μm, and single eumelanosomes were imaged at a field of view of 5 or 1.5 μm. The FEL spot size on the sample was ~30 × 100 μm. The images were digitally acquired and a procedure to determine the integrated emission intensity $S(\lambda)$ was developed. The procedure involved acquiring a histogram of the intensity for the relevant sections of each image, assuring that the image was not saturated and accounting for the laser power and the experimental and software gain settings of the image system.

The wavelength-dependent data reveal the relative photoioniza-tion quantum yield and the Fowler equation can be used to calculate the threshold photoionization potential (129):

$$S(\lambda)^{1/2} = C(h\nu - \Phi) \qquad (3)$$

where C is a constant that depends on the particular material, Φ is the threshold photoionization potential and $h\nu$ is the photon energy. If a plot of $S(\lambda)^{1/2}$ as a function of $h\nu$ is linear, then the threshold photoionization potential Φ is obtained by determining the value of ν where $S(\lambda)^{1/2} \rightarrow 0$.

Single melanosomes as well as aggregates were observed. Hair eumelanosomes tend to aggregate more upon drying than the
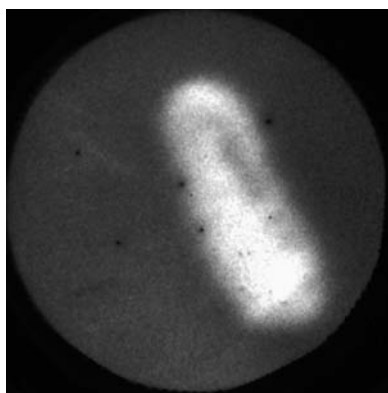
Figure 27. PEEM image of a single bovine eye melanosome: field of view = 1.5 μm, hν = 240 nm. The black spots are the result of damaged areas of the image intensifier (114).
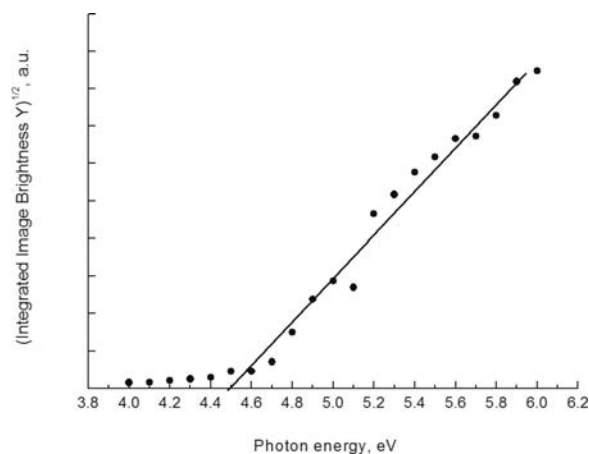

Figure 28. Square root of the brightness of the PEEM image $S^{1/2}$ of black human hair melanosomes plotted as a function of excitation wavelength. Extrapolation of $S(\lambda)^{1/2} \to 0$ gives a value for the threshold photo ionization potential of ~4.6 ± 0.2 eV (114).

bovine RPE melanosomes. Figure 27 shows a PEEM image of a single bovine eye melanosome at a field of view of 1.5 μm, demonstrating that high-resolution images of single melanosomes can be obtained. The elongated shape with aspect ratio of about 3 is well visualized. The dark strip parallel to the long axis of the eumelanosome is attributed to a shadowing effect in PEEM.

To collect sufficient PEEM signals to carry out the determination of the threshold photoionization potential, an aggregate of eumelanosomes was imaged, and the $S(\lambda)$ for the total image was determined. These studies were restricted to the black-hair eumelanosomes. The wavelength-dependent threshold photoelectron spectrum using the full tuning range of the FEL is shown in Fig. 28. The $S(\lambda)^{1/2}$ shows an essentially linear dependence on hν, and extrapolating to 0 gives a threshold photoionization potential of ~4.6 ± 0.2 eV. Various aggregates of eumelanosomes were examined, and the results were independent of the particular aggregate studied. Considering effects because of roughness, the observed value of threshold photoionization could be reduced by ~300 meV.

In the FEL-PEEM experiment, the melanosomes are photoionized under vacuum, and thus the photoionization potential is referenced to the vacuum level. The potential of an electron at rest in vacuum corresponds to –4.44 V *versus* the normal hydrogen electrode (NHE) (130). Therefore, we can deduce the oxidation potential of eumelanosomes *versus* the NHE as ~ –0.2 V. Moreover, electrochemical oxidation of 5,6-dihydroxyindole-melanin and voltammetric measurements of synthetic dopamine melanin provided results in reasonable agreement with that determined in the present study for intact eumelanosome (131,132).

Current and future enhancements of UV-FEL PEEM

The OK-4 optical klystron of the current storage-ring FEL at Duke University is to be replaced by the OK-5 optical klystron, to be summarized in the following section. The OK-5 will deliver both linear and circular polarizations, where the OK-4 produced only linear polarization, and extend UV operation to 150 nm and shorter wavelengths. The tunable and selectively polarizable OK-5 FEL will provide novel contrast mechanisms for future PEEM investigations.

Summary of UV FEL PEEM applications

The results summarized here demonstrate the significant accomplishments and the potential of the UV-FEL PEEM for nanoscale characterization of materials and nanoscale phenomena. The PEEM technique has the unique capability of real-time imaging over a wide range of conditions, and the tunable 3–7 eV UV FEL excitation allows spectroscopic imaging of individual metallic, semiconducting and biological nanostructures and the phenomena that involve these nanostructures.

FEL DEVELOPMENT AND POTENTIAL FOR APPLICATIONS RESEARCH

FEL light-source development continues throughout the spectrum (3–14). The Duke storage-ring FEL is an example of an FEL development project that in the near term promises novel light-source capabilities for applications research in the biological and material sciences. In the recent past, the optical klystron (OK-4) storage-ring FEL has produced UV light and via intracavity Compton backscattering has also produced gamma rays (133,134). The wavelengths of the UV photons and the gamma rays are tunable, determined by the energy of the stored electron beam and the properties of the magnetic fields produced by the optical klystrons. By 2006, the helical OK-5 will completely replace the linear OK-4 as shown in Fig. 29. The OK-5 storage-ring FEL will deliver circular, elliptical or linearly polarized light, where the OK-4 storage-ring FEL produced only linear polarization. The OK-5 storage-ring FEL is expected to extend UV operation from the current 193 nm produced with the OK-4 to 150 nm and shorter wavelengths. The OK-5 storage-ring FEL will extend the gamma ray range from the 60 MeV produced with the OK-4 to as high as 160 MeV.

The OK-5 storage-ring FEL will provide selectively polarizable UV light to the PEEM, summarized in the previous section, accessing novel contrast mechanisms. In addition, two time-resolved spectroscopic beamlines are in development for UV applications research. One two-color technique uses the storage-ring FEL as a pulsed UV source to excite electronic transitions and the downstream bending magnet as a broadband IR source to monitor the vibrational spectrum during the subsequent relaxation processes (135). The second time-resolved technique supports investigations based on UV-resonant Raman spectroscopy and photoluminescence measurements. In both cases, the tunable and
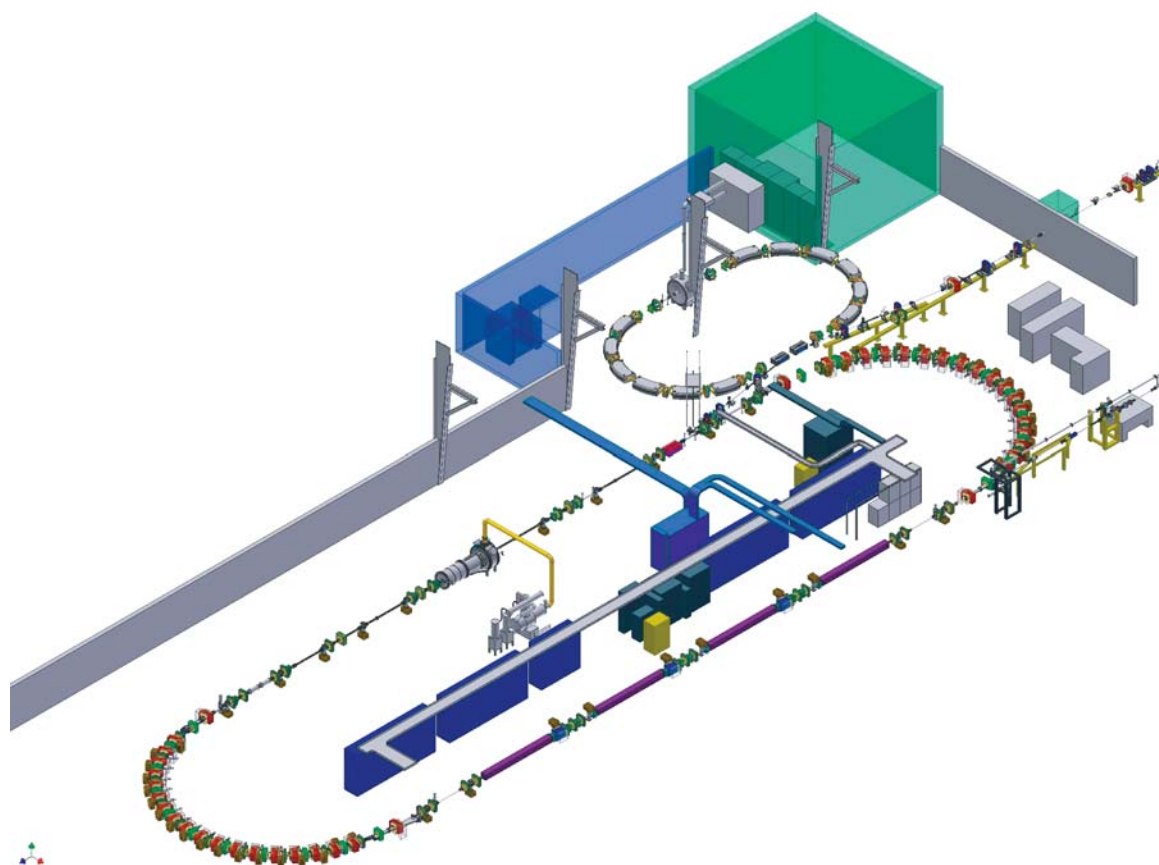
Figure 29. Schematic of the OK-5 storage-ring FEL. Four distributed optical klystrons of the OK-5 are shown in the lower-right straight section. Figure produced by Matthew Busch.

selectively polarizable OK-5 storage-ring FEL will allow novel access to previously disallowed quantum transitions in the UV. The nuclear physics community also has strong interests in the OK-5 storage ring FEL (14), which similarly will provide novel access to previously disallowed quantum transitions in the gamma ray regime.

The accelerator physics community has substantial interest in X-ray FELs that operate by the process of self-amplified spontaneous emission (SASE) (136,137). The successful demonstration of the SASE process in the IR, vis and UV regimes paves the way for the march to X-rays (138–142). X-ray SASE FEL development is a national laboratory-scale project and there is substantial interest worldwide including the TeV-energy superconducting linear accelerator (TESLA) at Deutsches Elektronen-Synchrotron (DESY, Hamburg, Germany) and the linac coherent light source (LCLS) at the Stanford Linear Accelerator Center (Menlo Park, CA) (143,144). Potential applications enabled by tunable, ultrashort X-rays with extremely high flux are quite intriguing (145).

CONCLUDING REMARKS

We have presented representative examples of FEL applications research in the biological and biomedical sciences and condensed matter and material research. THz, IR and UV FEL have been essential for pioneering physical techniques, including vibrational photon-echo spectroscopy, IR-REMPE, IR and two-color MALDI, IR-MAPLE, and UV-PEEM. FEL applications research has led to advances in electro-optics; coherent quantum control; photon-assisted transport; material and device physics; dynamical processes in amorphous materials, spintronics, nanostructures and nanocrystals, (bio)molecules, fullerenes, clusters and complexes; IR analysis and processing of organic materials; laser medicine; fracture dynamics; and nanoscale characterization of (bio)materials and nanoscale phenomena. FEL development continues to extend the light-source frontiers.

REFERENCES

1. Motz, H., W. Thon and R. N. Whitehurst (1953) Experiments on radiation by fast electron beams. *J. Appl. Phys.* **24**, 826–833.
2. Madey, J. M. J. (1971) Stimulated emission of bremsstrahlung in a periodic magnetic field. *J. Appl. Phys.* **42**(5), 1906–1913.
3. Marshall, T. C. (1985) *Free-Electron Lasers.* Macmillan, New York.
4. Brau, C. A. (1988) Free-electron lasers. *Science* **239**, 1115–1121.
5. Brau, C. A. (1990) *Free-Electron Lasers.* Academic, Boston.
6. Luchini, P. and H. Motz (1990) *Undulators and Free-Electron Lasers.* Clarendon, Oxford.
7. Freund, H. P. and T. M. Antonsen Jr. (1996) *Principles of Free-Electron Lasers*, 2nd ed. Chapman & Hall, London.
8. O'Shea, P. O. and H. P. Freund (2001) Free-electron lasers: status and applications. *Science* **292**, 1853.
9. National Research Council (1994) *Report of the Committee on Free Electron Lasers* National Academy, Washington, DC.
10. Colson, W. B., E. D. Johnson, M. J. Kelley and H. A. Schwettman (2002) Putting free-electron lasers to work. *Physics Today* **55**, 35–41.
11. Feder, T. (2002) Duke beams hard gamma rays, soft X rays. *Physics Today* **55**, 26–27.

12. Proceedings of the THz-Bridge Workshop, *J. Biol. Phys.* See issues **2** and **3** (2003).

13. Edwards, G. S., R. H. Austin, F. E. Carroll, M. L. Copeland, M. E. Couprie, W. E. Gabella, R. F. Haglund, B. A. Hooper, M. S. Hutson, E. D. Jansen, K. M. Joos, D. P. Kiehart, I. Lindau, J. Miao, H. S. Pratisto, J. H. Shen, Y. Tokutake, L. van der Meer and A. Xie (2003) Free-electron-laser-based biophysical and biomedical instrumentation. *Rev. Sci. Instruments* **74**, 3207–3245.

14. Weller, H. R. and M. W. Ahmed (2003) The HIγS facility: a free-electron laser generated gamma-ray beam for research in nuclear physics. *Modern Phys. Lett.* **A 18**, 1569–1590.

15. Publications of the UCSB Center for Terahertz Science and Technology. Available at: http://www.iquest.ucsb.edu/sites/sjallen/pubs/Through_2004.pdf. Accessed on 8 March 2005.

16. Franz, W. (1958) Einfluss eines elektrischen feldes auf eine optische absorptionskante. *Z. Naturforsch.* **13**, 484–489.

17. Keldysh, L. V. (1958) The effect of a strong electric field on the optical properties of insulating crystals. *Sov. Phys. J. Exp. Theor. Phys.* **34**, 788–790.

18. Nordstrom, K. B., K. Johnsen, S. J. Allen, A.-P. Jauho, B. Birnir, J. Kono, T. Noda, H. Akiyama and H. Sakaki (1998) Excitonic dynamical Franz-Keldysh effect. *Phys. Rev. Lett.* **81**, 457–460.

19. Carter, S. G, V. Ciulin, M. S. Sherwin, M. Hanson, M. Huntington, L. A. Coldren and A. C. Gossard (2004) Terahertz electro-optic wavelength conversion in GaAs quantum wells: improved efficiency and room-temperature operation. *Appl. Phys. Lett.* **84**, 840–842.

20. Cole, B. E., J. B. Williams, B. T. King, M. S. Sherwin and C. R. Stanley (2001) Coherent manipulation of semiconductor quantum bits with terahertz radiation. *Nature* **410**, 60–63.

21. Hegmann, F. A., J. B. Williams, B. Cole, M. S. Sherwin, J. W. Beeman and E. E. Haller, (2000) Time-resolved photoresponse of a gallium-doped germanium photoconductor using a variable pulse-width terahertz source. *Appl. Phys. Lett.* **76**, 262–264.

22. Keay, B. J., C. Aversa, S. Zeuner, S. J. Allen Jr., K. L. Campman, K. D. Maranowski, A. C. Gossard, U. Bhattacharya and M. J. W. Rodwell (1996) Virtual states, dynamic localization, absolute negative conductance and stimulated multiphoton emission in semiconductor superlattices. *Semiconductor Sci. Technol.* **11**, 1596–1600.

23. Keay, B. J., S. Zeuner, S. J. Allen Jr., K. D. Maranowski, A. C. Gossard, U. Bhattacharya and U. Rodwell (1995) Dynamic localization, absolute negative conductance, and stimulated, multiphoton emission in sequential resonant tunneling semiconductor superlattices. *Phys. Rev. Lett.* **75**, 4102–4105.

24. Holthaus, M. (1992) Collapse of minibands in far-infrared irradiated superlattices. *Phys. Rev. Lett.* **69**, 351–354.

25. Savvidis, P. G., B. Kolasa, G. Lee and S. J. Allen (2004) Resonant crossover of terahertz loss to the gain of a bloch oscillating in As/AlSB superlattice. *Phys. Rev. Lett.* **92**, 196802.

26. Jing Xu, J. Galan, G. Ramian, P. Savvidis, A. Scopatz, R. R. Birge, S. J. Allen and K. Plaxco (2003) Terahertz circular dichroism spectroscopy of biomolecules. In *Proceedings of the International Society of Optical Engineering,* Vol. 5268 (Edited by J. O. Jensen and J.-M. Theriault), pp. 19–26. SPIE, Providence.

27. Jing Xu, G. Ramian, J. F. Galan, P. G. Savvidis, A. M. Scopatz, R. R. Birge, S. J. Allen, W. Kevin and K. W. Plaxco (2003) Terahertz circular dichroism spectroscopy: a potential approach to the *in situ* detection of life's metabolic and genetic machinery. *Astrobiol. J.* **3**, 489–504.

28. Zimdars, D., A. Tokmakoff, S. Chen, S. R. Greenfield, M. D. Fayer, T. L. Smith and H. A. Schwettman (1993) Picosecond infrared vibrational photon echoes in a liquid and glass using a free electron laser. *Phys. Rev. Lett.* **70**, 2718–2721.

29. Tokmakoff, A. and M. D. Fayer (1995) Infrared photon echo experiments: exploring vibrational dynamics in liquids and glasses. *Acc. Chem. Res.* **20**, 437–445.

30. Rector, K. D. and M. D. Fayer (1998) Vibrational echoes: a new approach to condensed matter vibrational spectroscopy. *Int. Rev. Phys. Chem.* **17**, 261–306.

31. Fayer, M. D. (2001) Fast protein dynamics probed with infrared vibrational echo experiments. *Ann. Rev. Phys. Chem.* **52**, 315–356.

32. Farrar, T. C. and D. E. Becker (1974) *Pulse and Fourier Transform NMR.* Academic Press, New York.

33. Hahn, E. L. (1950) Spin echoes. *Phys. Rev.* **80**, 580–594.

34. Kurnit, N. A., I. D. Abella and S. R. Hartmann (1964) Observation of a photon echo. *Phys. Rev. Lett.* **13**, 567–568.

35. Abella, I., N. A. Kurnit and S. R. Hartmann (1966) Photon echoes. *Phys. Rev.* **141**, 391–406.

36. Tokmakoff, A., D. Zimdars, B. Sauter, R. S. Francis, A. S. Kwok and M. D. Fayer (1994) Vibrational photon echoes in a liquid and glass: room temperature to 10 K. *J. Chem. Phys.* **101**, 1741–1744.

37. Tokmakoff, A., A. S. Kwok, R. S. Urdahl, D. Zimdars and M. D. Fayer (1995) Multilevel vibrational dephasing and vibrational anharmonicity from infrared photon echo beats. *Chem. Phys. Lett.* **234**, 289–295.

38. Tokmakoff, A., R. S. Urdahl, D. Zimdars, R. S. Francis, A. S. Kwok and M. D. Fayer (1995) Vibrational spectral diffusion and population dynamics in a glass-forming liquid: variable bandwidth picosecond infrared spectroscopy. *J. Chem. Phys.* **102**, 3919–3931.

39. Hill, J. R., A. Tokmakoff, K. A. Peterson, B. Sauter, D. Zimdars, D. D. Dlott and M. D. Fayer (1994) Vibrational dynamics of carbon monoxide at the active site of myoglo-bin: picosecond infrared free-electron laser pump-probe experiments. *J. Phys. Chem.* **98**, 11213–11219.

40. Hill, J. R., D. D. Dlott, M. D. Fayer, K. A. Peterson, C. W. Rella, M. M. Rosenblatt, K. S. Suslick and C. J. Ziegler (1995) Vibrational relaxation of carbon monoxide in model heme compounds: 6-coordinate metalloporphyrins (M = Fe, Ru, Os). *Chem. Phys. Lett.* **244**, 218–223.

41. Dlott, D. D., M. D. Fayer, J. R. Hill, C. W. Rella, K. S. Suslick and C. J. Ziegler (1996) Vibrational relaxation in metalloporphyrin co complexes. *J. Am. Chem. Soc.* **118**, 7853–7854.

42. Rector, K. D., C. W. Rella, J. R. Hill, A. S. Kwok, S. G. Sligar, E. Y. P. Chien, D. D. Dlott and M. D. Fayer (1996) Tuning the vibrational relaxation of co-bound to heme and metal-loporphyrin complexes. *J. Phys. Chem.* **100**, 18023–18032.

43. Hill, J. R., D. D. Dlott, C. W. Rella, K. A. Peterson, S. M. Decatur, S. G. Boxer and M. D. Fayer (1996) Vibrational dynamics of carbon monoxide at the active sites of mutant heme proteins. *J. Phys. Chem.* **100**, 12100–12107.

44. Rella, C. W., A. S. Kwok, K. D. Rector, J. R. Hill, H. A. Schwettman, D. D. Dlott and M. D. Fayer (1996) Vibrational echo studies of protein dynamics. *Phys. Rev. Lett.* **77**, 1648–1651.

45. Rector, K. D., J. R. Engholm, C. W. Rella, J. R. Hill, D. D. Dlott and M. D. Fayer (1999) A Dynamical transition in the protein myoglobin observed by infrared vibrational echo experiments. *J. Phys. Chem. A* **103**, 2381–2387.

46. Rector, K. D., J. Jiang, M. Berg and M. D. Fayer (2001) Effects of solvent viscosity on protein dynamics: infrared vibrational echo experiments and theory. *J. Phys. Chem. B* **105**, 1081–1092.

47. Rector, K. D., C. W. Rella, J. R. Hill, A. S. Kwok, S. G. Sligar, E. Y. P. Chien, D. D. Dlott and M. D. Fayer (1997) Mutant and wild type myoglobin-co protein dynamics: vibrational echo experiments. *J. Phys. Chem. B* **101**, 1468–1475.

48. Oepts, D., A. F. G. van der Meer and P. W. van Amersfoort (1995) The free-electron laser user facility FELIX. *Infrared Phys. Technol.* **36**, 297–308.

49. van der Voort, M., C. W. Rella, L. F. G. van der Meer, A. V. Akimov and J. I. Dijkhuis (2000) Dynamics of Si-H vibrations in an amorphous environment. *Phys. Rev. Lett.* **84**, 1236–1239.

50. Wells, J.-P. R., R. E. I. Schropp, L. F. G. van der Meer and J. I. Dijkhuis (2002) Ultrafast vibrational dynamics and stability of deuterated amorphous silicon. *Phys. Rev. Lett.* **89**, 125504.

51. Wells, J.-P. R., P. J. Phillips, N. Tomozeiu, F. H. P. M. Habraken and J. I. Dijkhuis (2003) Infrared transient grating and photon echo spectroscopy of oxygen vibrational modes in amorphous silicon thin films. *Phys. Rev. B* **68**, 115207.

52. Ganichev, S. D., P. Schneider, V. V. Bel'kov, E. L. Ivchenko, S. A. Tarasenko, W. Wegschneider, D. Weiss, D. Schuh, B. N. Murdin, P. J. Phillips, C. R. Pidgeon, D. G. Clarke, M. Merrick, P. Murzyn, E. V. Beregulin and W. Prettl (2003) Spin-galvanic effect due to optical spin orientation. *Phys. Rev. B* **68**, 081302.

53. Xie, A., L. van der Meer, W. Hoff and R. H. Austin (2000) Long-lived amide I vibrational modes in myoglobin. *Phys. Rev. Lett.* **84**, 5435–5438.

54. Xie, A., A. F. G. van der Meer and R. H. Austin (2002) Excited-state lifetimes of far-infrared collective modes in proteins. *Phys. Rev. Lett.* **88**, 018102.

55. von Helden, G., D. van Heijnbergen and G. Meijer (2003) Resonant ionization using IR light: a new tool to study the spectroscopy and

dynamics of gas-phase molecules and clusters. *J. Phys. Chem. A* **107**, 1671–1688.

56. von Helden, G., I. Holleman, G. M. H. Knippels, A. F. G. van der Meer and G. Meijer (1997) Infrared resonance enhanced multiphoton ionization of fullerenes. *Phys. Rev. Lett.* **79**, 5234–5237.

57. von Helden, G., A. G. G. M. Tielens, D. van Heijnsbergen, M. A. Duncan, S. Hony, L. B. F. M. Waters and G. Meijer (2000) Titanium carbide nanocrystals in circumstellar environments. *Science* **288**, 313–316.

58. van Heijnsbergen, D., G. von Helden, M. A. Duncan, A. J. A. van Roij and G. Meijer (1999) Vibrational spectroscopy of gas phase metal carbide clusters and nanocrystals. *Phys. Rev. Lett.* **83**, 4983–4986.

59. Fielicke, A., G. von Helden, G. Meijer, B. Simard, S. Dénommée and D. M. Rayner (2003) Vibrational spectroscopy of CO in gas-phase rhodium cluster-CO complexes. *J. Am. Chem. Soc.* **125**, 11184–11185.

60. Fielicke, A., G. von Helden, G. Meijer, D. B. Peterson, B. Simard and D. M. Rayner (2004) Size and charge effects on the binding of CO to small isolated rhodium clusters. *J. Phys. Chem. B* **108**, 14591–14598.

61. Fielicke, A., A. Kirilyuk, C. Ratsch, J. Behler, M. Scheffler, G. von Helden and G. Meijer (2004) Structure determination of isolated metal clusters via far-infrared spectroscopy. *Phys. Rev. Lett.* **93**, 023401.

62. Asmis, K. R., N. L. Pivonka, G. Santambrogio, M. Brümmer, C. Kaposta, D. M. Neumark and L. Wöste (2003) Gas-phase infrared spectrum of the protonated water dimer. *Science* **299**, 1375–1377.

63. Oomens, J., D. T. Moore, G. von Helden, G. Meijer and R. C. Dunbar (2004) The site of Cr^+ attachment to gas-phase aniline from infrared spectroscopy. *J. Am. Chem. Soc.* **126**, 724–725.

64. Moore, D. T., J. Oomens, L. van der Meer, G. von Helden, G. Meijer, J. Valle, A. G. Marshall and J. R. Eyler (2004) Probing the vibrations of shared, OH^+O-bound protons in the gas phase. *Chem. Phys. Chem.* **5**, 740–743.

65. Bakker, J. M., L. Mac Aleese, G. Meijer and G. von Helden (2003) Fingerprint IR spectroscopy to probe amino acid conformations in the gas phase. *Phys. Rev. Lett.* **91**, 203003.

66. Jockusch, R. A., R. T. Kroemer, F. O. Talbot, L. C. Snoek, P. Çarçabal, J. P. Simons, M. Havenith, J. M. Bakker, I. Compagnon, G. Meijer and G. von Helden (2004) Probing the glycosidic linkage: UV and IR ion-dip spectroscopy of a lactoside. *J. Am. Chem. Soc.* **126**, 5709–5714.

67. Bakker, J. M., I. Compagnon, G. Meijer, G. von Helden, M. Kabeláč, P. Hobza and M. S. de Vries (2004) The mid-IR absorption spectrum of gas-phase clusters of the nucleobases guanine and cytosine. *Phys. Chem. Chem. Phys.* **6**, 2810–2815.

68. Militsyn, B. L., G. von Helden, G. J. M. Meijer and A. F. G. van der Meer (2003) FELICE—the free-electron laser for intracavity experiments. *Nucl. Instr. Meth. Phys. Res. A* **507**, 494–497.

69. Edwards, G. S., D. Evertson, W. Gabella, R. Grant, T. L. King, J. Kozub, M. Mendenhall, J. Shen, R. Shores, S. Storms and R. Traegar (1996) Free-electron lasers: reliability, performance, and beam delivery. *IEEE J. Special Topics in Quantum Electronics* **2**(4), 810–817.

70. Berkenkamp, S., F. Kirpekar and F. Hillenkamp (1998) Infrared MALDI mass spectrometry of large nucleic acids. *Science,* **281**(5374), 260–262.

71. Cramer, R., W. J. Richter, E. Stimson and A. L. Burlingame (1998) Analysis of phospho- and glycopolypeptides with infrared matrix-assisted laser desorption and ionization. *Anal. Chem.* **70**(23), 4939–4944.

72. Budnik, B. A., K. B. Jensen, T. J. D. Jorgenson, A. Haas and R. A. Zubarev (2000) Benefits of 2.94-µm infrared matrix-assisted laser desorption/ionization for analysis of labile molecules by Fourier transform mass spectrometry. *Rapid Commun. Mass Spectrom.* **14**(7), 578–584.

73. Strupat, K., M. Karas, F. Hillenkamp, C. Eckerskorn and F. Lottspeich (1994) Matrix-assisted laser-desorption ionization mass-spectrometry of proteins electroblotted after polyacrylamide-gel electrophoresis. *Anal. Chem.* **66**(4), 464–470.

74. Lippa, T., N. I. Taranenko, V. M. Doroshenko and C. R. Prasad (2002) Infrared matrix-assisted laser desorption/ionization quadrupole ion trap mass spectrometry. *Eur. J. Mass Spectrom.* **8**(3), 263–271.

75. Cramer, R. and A. L. Burlingame (2000) IR-MALDI—softer ionization in MALDI-MS for studies of labile macromolecules, In *Mass Spectrometry in Biology and Medicine* (Edited by A. L. Burlingame, S. A. Carr and M. A. Baldwin), pp. 289–307. Humana Press, Totowa, New Jersey.

76. Baltz-Knorr, M. L., K. E. Schriver and R. F. Haglund (2002) Infrared laser ablation and ionization of water clusters and biomolecules from ice. *Appl. Surface Sci.* **197–198**, 11–16.

77. Baltz-Knorr, M., D. R. Ermer, K. E. Schriver and R. F. Haglund Jr. (2002) Infrared laser desorption and ionization of polypeptides from a polyacrylamide gel. *J. Mass Spectrom.* **37**(3), 254–258.

78. Gross, J. and K. Strupat (1997) Matrix-assisted laser desorption/ ionisation mass spectrometry applied to biological macromolecules. *TrAc-Trends Anal. Chem.* **17**(8–9), 470–484.

79. Berkenkamp, S., C. Menzel, M. Karas and F. Hillenkamp (1997) Performance of infrared matrix-assisted laser desorption/ionization mass spectrometry with lasers emitting in the 3-µm wavelength range. *Rapid Commun. Mass Spectrom.* **11**(13), 1399–1406.

80. Little, M. W., J. K. Kim and K. K. Murray (2003) Two-laser infrared and ultraviolet matrix-assisted laser desorption/ionization. *J. Mass Spectrom.* **38**(7), 772–777.

81. Stryer, L. (1995) *Biochemistry,* 4th ed., W.H. Freeman, New York, 1064 p.

82. Klassen, J. S., S. G. Anderson and A. T. Blades (1996) Reaction enthalpies for $M^+L = M^+ + L$, where $M^+ = Na^+$ and K^+ and L = acetamide, *n*-methylacetamide, *N,N*-dimethylacetamide, glycine, and glycylglycine, from determinations of the collision-induced dissociation thresholds. *J. Phys. Chem.* **100**, 14218–14227.

83. Griffith, D. A. and A. M. Pajor (1999) Acidic residues involved in cation and substrate interactions in the Na+/dicarboxylate cotransporter, NaDC-1. *Biochemistry* **38**(23), 7524–7531.

84. Guo, B. C., B. J. Conklin and A. W. Castleman Jr. (1989) Thermochemical properties of ion complexes $Na^+(M)n$ in the gas phase. *J. Am. Chem. Soc.* **111**(17), 6506–6510.

85. Zhang, J., T. K. Ha, R. Knochenmuss and R. Zenobi (2002) Theoretical calculation of gas-phase sodium binding energies of common MALDI matrices. *J. Phys. Chem. A* **106**(28), 6610–6617.

86. Zhang, J., R. Knochenmuss, E. Stevenson and R. Zenobi (2002) The gas-phase sodium basicities of common matrix-assisted laser desorption/ionization matrices. *Int. J. Mass Spectrom.* **213**(2–3), 237–250.

87. Ohanessian, G. (2002) Interaction of MALDI matrix molecules with Na^+ in the gas phase. *Int. J. Mass Spectrom.* **219**(3), 577–592.

88. Nielen, M. W. F. (1999) MALDI time-of-flight mass spectrometry of synthetic polymers. *Mass Spectrom. Rev.* **18**(5), 309–344.

89. Harvey, D. J. (1999) Matrix-assisted laser desorption/ionization mass spectrometry of carbohydrates. *Mass Spectrom. Rev.* **18**(6), 349–450.

90. Goheen, S. C., K. L. Wahl, J. A. Campbell and W. P. Hess (1997) Mass spectrometry of low molecular mass solids by matrix-assisted laser desorption/ionization. *J. Mass Spectrom.* **32**(8), 820–828.

91. Karas, M., A. Ingedoh, U. Bahr and F. Hillenkamp (1989) Ultraviolet-laser desorption/ionization mass spectrometry of femtomolar amounts of large proteins. *Biomed. Environ. Mass Spectrom.* **18**(9), 841–843.

92. Dubois, F., R. Knochenmuss, R. J. J. M. Steenvoorden, K. Breuker and R. Zenobi (1996) On the mechanism and control of salt-induced resolution loss in matrix-assisted laser desorption/ionization. *Eur. Mass Spectrom.* **2**(2-3), 167–172.

93. Zhang, W. Z., S. F. Niu and B. T. Chait (1998) Exploring infrared wavelength matrix-assisted laser desorption/ionization of proteins with delayed-extraction time- of-flight mass spectrometry. *J. Am. Soc. Mass Spectrom.* **9**(9), 879–884.

94. Meacham, J. E., R. J. Cash, D. R. Dickinson, F. R. Reich, J. M. Grisby, A. K. Postma and M. A. Lilga (1996) *Safety Criteria for the Organic Watch List Tanks at the Hanford Site.* Westinghouse Hanford Company, Richland, WA, pp. 1–230.

95. Hess, W. P., H. K. Park, O. Yavas and R. F. Haglund Jr. (1998) IR-MALDI of low molecular weight compounds using a free electron laser. *Appl. Surface Sci.* **127–129**, 235–241.

96. Papantonakis, M. R., D. R. Ermer and R. F. Haglund Jr. (2002) Picosecond infrared matrix-assisted laser desorption/ionization mass spectrometry of organic molecules on sodium nitrate crystallites. *Appl. Surface Sci.* **197–198**, 213–216.

97. Haglund Jr., R. F., M. Baltz-Knorr, D. R. Ermer, M. R. Papantonakis and K. E. Schriver (2003) Laser mass spectrometry at high vibrational excitation density. *Spectrochimica Acta B,* **58**, 1125–1146.

98. Park, I. S. and N. Kim (1998) Thiolated Salmonella antibody immobilization onto the gold surface of piezoelectric quartz crystal. *Biosens. Bioelectron.* **13**(10), 1091–1097.

99. Grogan, C., R. Raiteri, G. M. O'Connor, T. J. Glynn, V. Cunningham, M. Kane, M. Charlton and D. Leech (2002) Characterisation of an antibody coated microcantilever as a potential immuno-based biosensor. *Biosens. Bioelectron.* **17**(3), 201–207.

100. Pique, A., R. A. McGill, D. B. Chrisey, D. Leonhardt, T. E. Mslna, B. J. Spargo, J. H. Callahan, R. W. Vachet, R. Chung and M. A. Bucaro (1999) Growth of organic thin films by the matrix assisted pulsed laser evaporation (MAPLE) technique. *Thin Solid Films* **356**, 536–541.

101. Haglund, R. F. Jr., D. M. Bubb, D. R. Ermer, J. S. Horwitz, E. J. Houser, G. K. Hubler, B. Ivanov, M. R. Papantonakis, B. R. Ringeisen and K. E. Schriver (2003) Resonant infrared laser materials processing at high vibrational excitation density: applications and mechanisms. In *Laser Precision Micromanufacturing,* Vol. 5063 (Edited by A. Ostendorf, H. Helvajian and K. Sugioka), pp. 13–23. Proceedings of the International Society of Optical Engineering, Munich.

102. Bubb, D. M., D. B. Chrisey, M. R. Papantonakis, R. F. Haglund Jr., J. S. Horwitz, R. A. McGill and B. Toftmann (2001) Resonant infrared pulsed-laser deposition of a sorbent chemoselective polymer. *Appl. Phys. Lett.* **79**(17), 2847–2849.

103. Gamaly, E. G., A. V. Rode and B. Luther-Davies (1999) Ultrafast ablation with high-pulse-rate lasers, part I: theoretical considerations. *J. Appl. Phys.* **85**(8), 4213–4221.

104. Rode, A. V., B. Luther-Davies, V. Z. Kolev, M. J. Lederer, N. R. Madsen, J. Giesekus, K.-M. Du and M. Duering (2004) Table-top 50W laser system for ultra-fast laser ablation. In *Appl. Phys. A* **79**, 1051–1055. 7th International Conference on Laser Ablation. 2003 Hersonissos, Crete, Greece.

105. Edwards, G., R. Logan, M. Copeland, L. Reinisch, J. Davidson, J. B. Johnson, R. Maciunas, M. Mendenhall, R. Ossoff, J. Tribble, J. Werkhaven and D. O'Day (1994) Tissue ablation by a free-electron laser tuned to the amide II band. *Nature* **371**, 416–419.

106. See reference 13, sections II–VI, pp. 3208–3221, and references therein.

107. Hutson, M. S., S. A. Hauger and G. Edwards (2002) Thermal diffusion and chemical kinetics in laminar biomaterial due to heating by a free-electron laser. *Phys. Rev. E* **65**, 061906.

108. Hutson, M. S. and G. S. Edwards (2005) Advances in the physical understanding of laser surgery at 6.45 microns. *Phys. Rev. ST AB* Proceedings of the 11th FEL Users Workshop (Trieste, Italy).

109. Copeland, M. L., R. J. Maciunas and G. S. Edwards (1998) Use of the free-electron laser for metastatic brain tumors. In *Neurosurgical Topics: Advanced Techniques in Central Nervous System Metastases* (Edited by R. J. Maciunas), pp. 113–121. The American Association of Neurological Surgeons, Park Ridge, IL.

110. Sun, W., J. H. Shen, D. J. Shetlar and K. M. Joos (2000) Endoscopic goniotomy with the free electron laser in congenital glaucoma rabbits. *J. Glaucoma* **9**, 325–333.

111. Ade, H., W. Yang, S. L. English, J. Hartman, R. F. Davis and R. J. Nemanich (1998) A free electron laser–photoemission electron microscope system (FEL-PEEM). *Surf. Rev. Lett.* **5**, 1257–1268.

112. Yang, W.-C., M. Zeman, H. Ade and R. J. Nemanich (2003) Attractive migration and coalescence: a significant process in the coarsening of TiSi$_2$ islands on the Si(111) surface. *Phys. Rev. Lett.* **90**, 136102.

113. Yang, W-C., B. J. Rodriguez, M. Park, R. J. Nemanich, O. Ambacher and V. Cimalla (2003) Photoelectron emission microscopy observation of inversion domain boundaries of GaN-based lateral polarity heterostructures. *J. Appl. Phys.* **94**, 5720–5725.

114. Samokhvalov, A., J. Garguilo, W.-C. Yang, G. S. Edwards, R. J. Nemanich and J. D. Simon (2004) Photoionization threshold of eumelanosomes determined using UV-free electron laser-photoelectron emission microscopy. *J. Phys. Chem. B* **108**, 16334–16338.

115. Shchuki, W. A. and D. Bimberg (1999) Spontaneous ordering of nanostructures on crystal surfaces. *Rev. Mod. Phys.* **71**, 1125–1171.

116. Zinke-Allmang, M., L. C. Feldman and M. H. Grabow (1992) Clustering on Surfaces. *Surf. Sci. Rep.* **16**, 377–463.

117. Zinke-Allmang, M. (1999) Phase separation on solid surfaces: nucleation, coarsening and coalescence kinetics. *Thin Solid Films* **346**, 1–68.

118. Theis, W., N. C. Bartelt and R. M. Tromp (1995) Chemical potential maps and spatial correlations in 2D-island ripening on Si(001). *Phys. Rev. Lett.* **75**, 3328–3331.

119. Rosenfeld, G., K. Morgenstern, M. Esser and G. Comsa (1999) Dynamics and stability of nanostructures on metal surfaces. *Appl. Phys. A* **69**, 489–496.

120. Ambacher, O., J. Smart, J. R. Shealy, N. G. Weimann, K. Chu, M. Murphy, R. Dimitrov, L. Wittmer, M. Wittmer, M. Stutzmann, W. Rieger and J. Hilsenbeck (1999) Two-dimensional electron gases induced by spontaneous and piezoelectric polarization charges in N- and Ga-face AlGaN/GaN heterostructures. *J. Appl. Phys.* **85**, 3222–3233.

121. Griffith, O. H., G. H. Lesch, G. F. Rempfer, G. B. Birrell, C. A. Burke, D. W. Schlosser, M. H. Mallon, G. B. Lee, R. G. Stafford, P. C. Jost and T. B. Marriott (1972) Photoelectron microscopy—new approach to mapping organic and biological surfaces. *Proc. Nat. Acad. Sci. USA* **69**, 561–565.

122. Birrell, G. B., D. L. Habliston and O. H. Griffith (1994) Photoelectron imaging of viruses and DNA—evaluation of substrates by unidirectional low-angle shadowing and photoemission current measurements. *Biophys. J.* **67**, 2041–2047.

123. Griffith, O. H. and G. F. Rempfer (1985) Photoelectron imaging in cell biology. *Ann. Rev. Biophys. Biophys. Chem* **14**, 113–160.

124. Habliston, D. L., K. K. Hedberg, G. B. Birrell, G. F. Rempfer and O. H. Griffith (1995) Photoelectron imaging of cells—photoconductivity extends the range of applicability. *Biophys. J.* **69**, 1615–1624.

125. Birrell, G. B., K. K. Hedberg, D. L. Habliston, and O. H. Griffith (1991) Biological applications of photoelectron imaging: a practical perspective. *Ultramicroscopy* **36**, 235–251.

126. Dam, R. J., K. K. Nadakavukaren and O. H. Griffith (1977) Photoelectron microscopy of cell-surfaces. *J. Microscopy* **111**, 211–217.

127. Griffith, O. H., D. L. Holmbo, D. L. Habliston and K. K. Nadakavukaren (1981) Contrast effects in photoelectron microscopy; UV dose-dependent quantum yields of biological surface components. *Ultramicroscopy* **6**, 149–156.

128. Liu, Y. and J. D. Simon (2003) Isolation and biophysical studies of natural eumelanins: applications of imaging technologies and ultrafast spectroscopy. *Pigm. Cell Res.* **16**, 606–618.

129. Rapp, M. and F.-J. Luebken (1999) Modelling of positively charged aerosols in the polar summer mesopause region. *Earth Planets Space* **51**, 799–807.

130. Graetzel, M. (2001) Photoelectrochemical cells. *Nature* **414**, 338–344.

131. Serpentini, C.-L., C. Gauchet, D. de Montauzon, M. Comtat, J. Ginestar and N. Paillous (2000) First electrochemical investigation of the redox properties of DOPA-melanins by means of a carbon paste electrode. *Electrochim. Acta* **45**, 1663–1668.

132. Nofsinger, J. B., S. E. Forest and J. D. Simon (1999) Explanation for the disparity among absorption and action spectra of eumelanin. *J. Phys. Chem. B* **103**, 11428–11432.

133. Litvinenko V. N., B. Burnham, M. Emamian, N. Hower, J. M. J. Madey, P. Morcombe, P. G. O'Shea, S. H. Park, R. Sachtschale, K. D. Straub, G. Swift, P. Wang, Y. Wu, R. S. Canon, C. R. Howell, N. R. Roberson, E. C. Schreiber, M. Spraker, W. Tornow, H. R. Weller, I. V. Pinayev, N. G. Gavrilov, M. G. Fedotov, G. N. Kulipanov, G. Y. Kurkin, S. F. Mikhalov, V. M. Popik, A. N. Skrinsky, N. A. Vinokurov, B. E. Norum, A. Lumpkin and B. Yang (1997) Gamma-ray production in a storage ring FEL. *Phys. Rev. Lett.* **78**, 4569–4572.

134. Litvinenko, V. L., S. H. Park, I. V. Pinayev and Y. Wu (2001) Performance of the OK-4, duke storage-ring free-electron laser. *Nucl. Instrum. Methods Phys. Res. A* **470**, 66–75.

135. See reference 13, section XII, pp. 3236–3239.

136. Kondratenko, M. and E. L. Saldin (1979) Generation of coherent radiation by a relativistic-electron beam in an undulator. *Sov. Phys. Dokl.* **24**, 986–988.

137. Bonifacio, R., C. Pellgrini and L. M. Narducci (1984) Collective instabilities and high-grain regimen in a free electron laser. *Opt. Commun.* **50**, 373–378.

138. Hogan, M. J., C. Pellegrini, J. Rosenzweig, S. Anderson, P. Frigola, A. Tremaine, C. Fortgang, D. C. Nguyen, R. L. Sheffield, J. Kinross–Wright, A. Varfolomeev, A. A. Varfolomeev, S. Tolmachev and R. Carr (1998) Measurements of gain larger that 10^5 at 12 μm in a self-amplified spontaneous laser. *Phys. Rev. Lett.* **81**, 4867–4870.

139. Babzien, M., I. Ben-Zvi, P. Catravas, J.-M. Fang, T. C. Marshall, X. J. Wang, J. S. Wurtele, V. Yakimenko, and L. H. Yu (1998)

Observation of self-amplified spontaneous emission in the near-IR and visible wavelengths. *Phys. Rev. E* **57**, 6093–6100.

140. Milton, S. V., E. Gluskin, S. G. Biedron, R. J. Dejus, P. K. Den Hartog, J. N. Galayda, K.-J. Kim, J. W. Lewellen, E. R. Moog, V. Sajaev, N. S. Sereno, G. Travish, N. A. Vinokurov, N. D. Arnold, C. Benson, W. Berg, J. A. Biggs, M. Borland, J. A. Carwardine, Y.-C. Chae, G. Decker, B. N. Deriy, M. J. Erdmann, H. Friedsam, C. Gold, A. E. Grelick, M. W. Hahne, K. C. Harkay, Z. Huang, E. S. Lessner, R. M. Lill, A. H. Lumpkin, O. A. Makarov, G. M. Markovich, D. Meyer, A. Nassiri, J. R. Noonan, S. J. Pasky, G. Pile, T. L. Smith, R. Soliday, B. J. Tieman, E. M. Trakhtenberg, G. F. Trento, I. B. Vasserman, D. R. Walters, X. J. Wang, G. Wiemerslage, S. Xu and B.-X. Yang, (2000) Observation of self-amplified spontaneous emission and exponential growth at 530 nm. *Phys. Rev. Lett.* **85**, 988–991.

141. Andruszkow, J., B. Aune, V. Ayvazyan, N. Baboi, R. Bakker, V. Balakin, D. Barni, A. Bazhan, M. Bernard, A. Bosotti, J. C. Bourdon, W. Brefeld, R. Brinkmann, S. Buhler, J.-P. Carneiro, M. Castellano, P. Castro, L. Catani, S. Chel, Y. Cho, S. Choroba, E. R. Colby, W. Decking, P. Den Hartog, M. Desmons, M. Dohlus, D. Edwards, H. T. Edwards, B. Faatz, J. Feldhaus, M. Ferrario, M. J. Fitch, K. Flöttmann, M. Fouaidy, A. Gamp, T. Garvey, C. Gerth, M. Geitz, E. Gluskin, V. Gretchko, U. Han, W. H. Hartung, D. Hubert, M. Hüning, R. Ischebek, M. Jablonka, J. M. Joly, M. Juillard, T. Junquera, P. Jurkiewicz, A. Kabel, J. Kahl, H. Kaiser, T. Kamps, V. V. Katalev, J. L. Kirchgessner, L. Körfer, L. Kravchuk, G. Kreps, J. Krzywinski, T. Lokajczyk, R. Lange, B. Leblond, M. Leenan, J. Lesrel, M. Liepe, A. Liero, T. Limberg, R. Lorenz, Lu Lui Hua, Lu Fu Hai, C. Magne, M. Maslov, G. Materlik, A. Matheisen, J. Menzel, P. Michelato, W.-D. Möller, A. Mosnier, U.-C. Müller, O. Napoly, A. Novokhatski, M. Omeich, H. S. Padamsee, C. Pagani, F. Peters, B. Petersen, P. Pierini, J. Pflüger, P. Piot, B. Phung Ngoc, L. Plucinski, D. Proch, K. Rehlich, S. Reiche, D. Reschke, I. Reyzl, J. Rosenzweig, J. Rossbach, S. Roth, E. L. Saldin, W. Sandner, Z. Sanok, H. Schlarb, G. Schmidt, P. Schmüser, J. R. Schneider, E. A. Schneidmiller, H.-J. Schreiber, S.

Schreiber, P. Schütt, J. Sekutowicz, L. Serafini, D. Sertore, S. Setzer, S. Simrock, B. Sonntag, B. Sparr, F. Stephan, V. A. Sytchev, S. Tazzari, F. Tazzioli, M. Tigner, M. Timm, M. Tonutti, E. Trakhtenberg, R. Treusch, D. Trines, V. Verzilov, T. Vielitz, V. Vogel, G. V. Walter, R. Wanzenberg, T. Weiland, H. Weise, J. Weisend, M. Wendt, M. Werner, M. M. White, I. Will, S. Wolff, M. V. Yurkov, K. Zapfe, P. Zhogolev and F. Zhou (2000) First observation of self-amplified spontaneous emission in a free-electron laser at 109 nm wavelength. *Phys. Rev. Lett.* **85**, 3825–3829.

142. Milton, S.V., E. Gluskin, N. D. Arnold, C. Benson, W. Berg, M. Borland, Y.-C. Chae, R. J. Dejus, P. K. Den Hartog, B. Deriy, M. Erdmann, Y. I. Eidelman, M. W. Hahne, Z. Huang, K.-J. Kim, J. W. Lewellen, Y. Li, A. H. Lumpkin, O. Makarov and E. R. Moog, (2001) Exponential GaN and saturation of a self-amplified spontaneous emission free-electron laser. *Science* **292**, 2037–2041.

143. Brinkmann, R., G. Materlik, J. Rossbach and A. Wagner (1997) Conceptual design of a 500 GeV e+e linear collider with integrated X-ray laser facility DESY report DESY97-048, Deutsches Elektronen Synchrotron, Hamburg, Germany.

144. Cornacchia, M., J. Arthur, K. Bane, L. Bertolini, V. Bharadwaj, K. van Bibber, G. Bowden, R. Boyce, R. Carr, J. Clendenin, W. Corbett, T. Cremer, P. Emma, A. Fasso, W. Fawley, C. Field, A. Fisher, A. Freund, R. Gould, L. Griffith, K. Halbach, R. Hettel, D. Humphries, J. Humphrey, K.-J. Kim, K. Ko, T. Kotseroglou, Z. Li, M. Libkind, S. Lidia, T. Limberg, D. Martin, B. McSwain, D. Meyerhofer, R. Miller, R. Moore, C. Ng, H.-D. Nuhn, D. Palmer, C. Pellegrini, M. Pietryka, S. Rokni, J. Rosenzweig, R. Ruland, E. T. Scharlemann, R. Schlueter, J. Schmerge, S. Schriber, L. Serafini, R. Sheffield, J. Sheppard, R. Tatchyn, V. Vylet, D. Walz, R. Warnock, H. Winick, M. Woodley, M. Xie, A. Yeremian, R. Yotam and F. Zimmerman (1998) Linac Coherent Light Source (LCLS) design study report, revised 1998 report SLAC-R-521, Stanford Linear Accelerator Center, Stanford, CA.

145. See reference 13, section XIV, pp. 3241–3243.